Nature Geoscience
2021, Volume 14, Pages 787-795
https://doi.org/10.1038/s41561-021-00809-x
https://archimer.ifremer.fr/doc/00718/83007/

Birth of a large volcanic edifice offshore Mayotte via lithosphere-scale dyke intrusion

Feuillet Nathalie [1, *], Jorry Stephan [2], Crawford Wayne C. [1], Deplus Christine [1], Thinon Isabelle [3], Jacques Eric [1], Saurel Jean Marie [1], Lemoine Anne [3], Paquet Fabien [3], Satriano Claudio [1], Aiken Chastity [2], Foix Oceane [1], Kowalski Philippe [1], Laurent Angèle [1], Rinnert Emmanuel [2], Cathalot Cecile [2], Donval Jean-Pierre [2], Guyader Vivien [2], Gaillot Arnaud [2], Scalabrin Carla [2], Moreira Manuel [1], Peltier Aline [1], Beauducel François [1, 4], Grandin Raphaël [1], Ballu Valérie [5], Daniel Romuald [1], Pelleau Pascal [2], Gomez Jérémy [1], Besançon Simon [1], Geli Louis [2], Bernard Pascal [1], Bachelery Patrick [6], Fouquet Yves [2], Bertil Didier [3], Lemarchand Arnaud [1], Van Der Woerd Jérome [7]

[1] Université de Paris, Institut de physique du globe de Paris, CNRS, Paris, France
[2] IFREMER, Unité Géosciences Marines, Technopole La Pointe du Diable, Plouzané, France
[3] Bureau de Recherches Géologiques et Minières—BRGM, DGR/GBS, Orléans, France
[4] Université Grenoble Alpes, IRD, ISterre, Grenoble, France
[5] LIttoral ENvironnement et Sociétés (LIENSs) UMR7266, Université de La Rochelle—CNRS, La Rochelle, France
[6] Université Clermont Auvergne, CNRS, IRD, OPGC, Laboratoire Magmas et Volcans, Clermont-Ferrand, France
[7] Institut de Physique du Globe de Strasbourg UMR7516 CNRS Université de Strasbourg, Strasbourg, France

* Corresponding author : Nathalie Feuillet, email address : feuillet@ipgp.fr

Abstract :

Volcanic eruptions shape Earth's surface and provide a window into deep Earth processes. How the primary asthenospheric melts form, pond and ascend through the lithosphere is, however, still poorly understood. Since 10 May 2018, magmatic activity has occurred offshore eastern Mayotte (North Mozambique channel), associated with large surface displacements, very-low-frequency earthquakes and exceptionally deep earthquake swarms. Here we present geophysical and marine data from the MAYOBS1 cruise, which reveal that by May 2019, this activity formed an 820-m-tall, ~5 km³ volcanic edifice on the seafloor. This is the largest active submarine eruption ever documented. Seismic and deformation data indicate that deep (>55 km depth) magma reservoirs were rapidly drained through dykes that intruded the entire lithosphere and that pre-existing subvertical faults in the mantle were reactivated beneath an ancient caldera structure. We locate the new volcanic edifice at the tip of a 50-km-long ridge composed of many other recent edifices and lava flows. This volcanic ridge is an extensional feature inside a wide transtensional boundary that transfers strain between the East African and Madagascar rifts. We propose that the massive eruption originated from hot asthenosphere at the base of a thick, old, damaged lithosphere.

Since May 10 2018, Mayotte Island (Comoros archipelago, Indian Ocean, *Figure 1a*) has experienced a major magmatic event off its eastern coast. This event generated more than 11000 detectable earthquakes (up to Mw 5.9), surface deformation rates of up to 200 mm/year and unusual very low frequency (VLF) earthquakes [1,2,3]. As of May 2021 (the time of writing), Mayotte is still deforming and both VLF events and earthquakes with Mw up to 4 are still being recorded.

Prior to this event, no recent eruption or significant seismic activity was reported around Mayotte [2]. Only two earthquakes were detected within 100 km of the island since 1972 [4] and the most recent volcanic exposure is a 4-6 kyr-old pumice layer sampled in the lagoon surrounding the island [5].

Recent geodynamic reconstructions suggest that the Comoros archipelago was built on ~150 Ma old oceanic lithosphere accreted to accommodate the opening of the Western Somali Basin [6]. The Comorian volcanism may result from partial melting of the base of this old lithosphere in interaction with plume material [7,8,9], possibly super plumes originating from Africa [10,11,12] , and may have been controlled by lithospheric deformation [13] [14]. Subaerial volcanic activity on Mayotte island began 11 My ago [13]. Well-preserved cones, tuff rings and maar craters in the Northeastern part of the island (on Petite Terre and in and around Mamoudzou [15,7] and further offshore [16] *(Figure 1b)* testify to relatively recent (probably Holocene, [7]) subaerial explosive volcanic activity. Gas emissions on Petite-Terre indicate magma degassing [17].

The discovery of the eruption and the new volcanic edifice

To determine the origin of the seismicity and deformation and to search for any seafloor volcanic activity, we deployed Ocean Bottom Seismometers (OBS) with attached Absolute Pressure Gauges (APG) and acquired high-resolution marine data (bathymetry, seafloor and water column backscatter), rock dredges and CTD (Conductivity-Temperature-Depth)- Rosette during the MAYOBS1 (2-19 May 2019) cruise aboard the R/V Marion Dufresne [18].

A systematic 12 kHz multibeam echosounder survey east of Mayotte, revealed a 820 m tall new volcanic edifice (NVE) 50 km east of Mayotte *(Figure 1)*. The NVE was detected by comparing our data to those acquired during a 2014 survey by the French Naval Hydrographic and Oceanographic Service (SHOM) [19] *(Figure 2a)*. The edifice sits on an area that, in the 2014 seafloor topography, was locally almost flat at around 3300 m below sea level (bsl).

The NVE has grown on the lower insular slope of Mayotte, at the eastern tip of a WNW-ESE trending volcanic ridge (Mayotte ridge) on the submarine flank of Mayotte (*Figure 1*). The NVE and many other volcanic features along the ridge have high acoustic reflectivity compared to the surrounding sediments, indicating recent volcanic activity all along the ridge *(Figure 1c and extended data Figures 1,2,3).* The ridge is 50 km long, extending from the most recent subaerial cones and maar craters on Grande-Terre and Petite-Terre islands (MPT Volcanic zone) to the NVE *(Figure 1b)*. It is divided into two main segments, one on the upper slope (western) and one on the mid- to lower-slope (eastern). The eastern segment trends N130°E and is made of many constructional features similar to mafic submarine eruption features observed elsewhere [20,21,22]: cones up to 2 km-wide and 500 m-high, probably monogenetic; lava flows with smooth bathymetry, elongated ridges with steep slopes and varying orientations, which could result from dykes in more sedimented areas *(Figure 1 and extended data Figure 2d,e)*.

The western segment is made of volcanic features having more complex morphologies and emplaced along different directions *(Figure 1b and extended data Figure 2b,c)*. The main features are: i) Two N40°E and N120°E trending sets of high-backscatter cones and lava flows, northeast and southeast of Petite-Terre, respectively. These sets converge toward the onshore maar craters of Petite-Terre and may have been emplaced along pre-existing fractures or faults; ii) a horse-shoe shaped edifice (the Horseshoe) with a 3.5 km wide cone, steep slopes and a large collapse-induced scar. East of the Horseshoe, several smaller cones and volcanic features are aligned E-W, suggesting eruptive fissures. Large lava flows originate from this fissure system. iii) a 4 km-wide circular structure (the Crown), whose rim is crowned by seven 1 km-wide, 100-150m high volcanic cones. Their arrangement suggests typical post-caldera domes [23]. West of the Crown, submarine canyons and slope failure scars terminate at a N-S trending slope break that may be controlled by faulting. The Crown appears to sit inside a larger 10 km wide flat depression, bounded by faults and fissures, which could be the remnant of an ancient caldera collapse.

The NVE is located at the eastern tip of the eastern segment of the Mayotte ridge *(Figures 1b)*. In May 2019, its summit rose to 2580 m bsl. Its central peak resembles a pyramid with steep and smooth slopes *(Figure 2a and extended data Figure 3)*. Radial ridges, up to 300 m thick and extending up to 5 km from the central pyramid, display hummocky morphology similar to that observed along mid-ocean volcanic ridges [24] and active seamounts [22] and probably correspond to coalesced pillow lava mounds [21]. Beyond and in-between the hummocky ridges, flat areas up to 100 m thick, with high backscatter, could indicate channelized lava flows or sheet flows emplaced at high effusion rates [25]. We calculate the volume of material corresponding to the 2014- 2019 seafloor depth difference to be at least 5.0 ± 0.3 km^3 *(Figure 2b).* Popping fragments of very fresh basanitic pillow lavas (SiO2 47 wt%, Na_20 + K_2O 7.1 wt%, MgO 5.7 wt% [26]) were dredged on the northeastern flank of the NVE, near its summit

(see *Figure 2a* for sample location and *supplementary S1)*. The lavas, similar to other basanites sampled in northern Mayotte [7] are aphyric with rare microphenocrysts of olivine (Fo70) and Ti-magnetite.

A ~1900-m high, vertical acoustic plume, rising through the water column from the NVE summit to ~800 m below the sea surface, was imaged several times during the cruise using the ship-borne multibeam echosounder (*Figure 3*, supplementary movie 1). A vertical CTD/rosette cast to 3137m depth above the northern flank of the NVE, 1000m offset from the summit, showed strong geochemical signatures. High volatile concentrations (H_2 = 550nM, CH_4 = 831 nM, CO_2= 34 µM), high turbidity and high total alkalinity values were associated with temperature and pH anomalies (respectively 0.2°C and 1 pH unit) [27] and *Extended data Fig. 4*). Such chemical anomalies are characteristic of submarine eruptions and may reflect magma degassing [28], molten lava interaction with seawater [29] or fluid/water discharge from subsurface storage zones in the crust or sedimentary cover [30]. The height and the strong backscatter signature of the acoustic plume suggest that a mixture of solid particles (pyroclastic/hyaloclastic jet [28]) and/or differentiated fluid phases (droplets, hydrate-coated bubbles or free gas [31]) are driven upward through the water column from the NVE summit [32]. High turbidity measured at water depths below 2500 m, on the northern flank of the NVE, likely indicates the presence of these particles [33]. Both the multiple observations of the vertical acoustic plume at the summit of the NVE and the high H_2 concentration 1 km away indicate that the eruption was likely on-going in May 2019 [29].

In the upper slope zone, 30 km away from the volcano, two, ~1000-m high acoustic plumes were detected above the Horseshoe edifice *(Figure 1 and extended data Figure 5, movie 2)* but no significant changes in seafloor morphology or reflectivity were detected.

The seismicity and VLF events relocated by OBS data

The combined land-OBS network of seismic stations (supplementary Figure S2.1) detected 17000 events between February 25 and May 6, 2019. We manually relocated about 800 of the largest earthquakes onboard (*see method and supplementary S2*). Ninety-four percent of the earthquakes cluster beneath the western segment of the Mayotte ridge, 40 km west of the NVE and 5 to 15 km east of Petite-Terre (swarm 1, *Figure 1*). Almost all of the remaining events form a secondary swarm beneath the northwestern tip of the eastern segment, 30 km from Petite-Terre and 20 km from the NVE (swarm 2, *Figure 1*). A few events are also scattered along the eastern segment. We searched the full OBS-land catalog for events beneath the NVE, but found none. The located earthquakes are all very deep, ranging from 25±5 to 50±5 km. In addition, all P-S arrival delays recorded by an OBS deployed for 48h above the main swarm were greater than 3 seconds, indicating no events less than 20 km depth *(Figure 4, extended data Figure 6b, method and supplementary S2.2).* The land-OBS catalog does not show any evidence for seismicity migration, but it only represents a two-month "snapshot" of the activity. To extend the observational time window, we relocated 139 earthquakes recorded by the land stations between May 2018 and the first OBS deployment. All the events were beneath the volcanic ridge *(extended data fig. 6a).* During the first weeks of the crisis, they were mainly located beneath the northwestern tip of the eastern segment, between 30 and 50 km depth, whereas in the last two weeks of June, a few events occurred closer to the NVE and between 30km-depth and the surface.

In addition to the high frequency seismicity, VLF events were recorded by the OBSs wideband hydrophones. Their waveforms are similar to those of the globally detected November 11 2018 event (exponentially decaying monochromatic signals of approximately 2000s duration, with dominant period of ~15 s and polarized Rayleigh waves), suggesting repeated excitation of the same radiating source. We located 84 VLF events using waveform cross-correlation *(see*

189 *method and supplementary S2.3)*, all of them are most probably above seismic swarm 1
190 *(Figures 4 and extended data Figure 6b)*, at a mean depth of 22 ± 15 km.
191
192 **GNSS data and APG modeling**
193 The GNSS network includes nine stations on Mayotte Island and two far field stations at Diego
194 Suarez and Grande Glorieuse islands. The geometry is not optimal, preventing geodetic
195 inversions for complicated structures or media. We performed Bayesian inversions [34] of the data
196 using a point source in an elastic half-space with two distinct analytical formalisms: an isotropic
197 point source [35] and a point compound dislocation model (pCDM, [36] *see method, supplementary*
198 *S3 and extended data Figure 7)*. In both cases, the results indicate ~5 km^3 deflation of a deep
199 reservoir (> 30 km). The simplest and most robust model is the deflation of ~ 40 km deep
200 isotropic source below the eastern segment of the Mayotte ridge. An increase in absolute
201 seafloor pressure measured by all APGs on the OBS frames, interpreted as seafloor subsidence,
202 is compatible with these models *(see method, supplementary S3, extended data Figure 7d)*.
203
204 **Magma reservoirs and chronology of the eruption**
205 Most of our located seismicity and modelled GNSS sources lie in the lithospheric mantle,
206 beneath the ~17 km deep Moho [37]. Volcanic seismicity this deep is rarely documented [38,39],
207 especially in dense swarms during eruptions.
208 The distribution of the seismicity in the first weeks of the crisis suggests a dyke migration from
209 the mid-slope zone to the NVE, along the eastern segment of the Mayotte ridge. This is also
210 supported by the migration of the largest earthquakes' Centroid Moment Tensor depths [40]
211 towards the surface *(extended data Figures 6c and 8)* and agrees well with [1,2]. The earthquakes
212 show strike-slip focal mechanisms compatible with a least compressive principal stress
213 orthogonal to the eastern segment of the ridge. Similar stress trends have been observed during
214 dyking events beneath the Izu peninsula in Japan [41] and in Iceland [42] but at much shallower

depths, where they were interpreted as seismic shear faulting caused by stress transfer to the surrounding vertical faults in response to dyke opening and propagation.

During the first six weeks of the crisis, the magma migrated 20 km laterally along the eastern segment of the Mayotte ridge, then upward (*Figure 4* and *extended data Figure 8*). The building of the NVE may have begun in July 2018, once the dyke reached close to the surface [2,1] allowing for high magma flow rates and rapid ensuing growth. On the basis of this assumption, we estimate a minimum mean lava flow rate of ~180m^3s^{-1} between the start of the eruption on the seafloor and our survey (~ 11 months). The local stress probably decreased considerably once the magma path to the NVE was opened, as is observed during many eruptions involving dyke propagation [43], which would explain why no earthquakes were detected beneath the NVE during the OBS deployment.

After the dike reached the near surface, seismicity resumed beneath the mid- and upper-slope volcanic zones *(Figure 4 and extended data Figures 6a,b and 8)* and its pattern appears to be constant since September 2018 [2]. This stationary seismicity could be caused by stress perturbation along pre-existing structures and/or fluid (gas, magma or water) motions. The swarm 1 earthquakes cluster beneath the ancient caldera structure inferred from our high-resolution bathymetry (*Figure 1c* and *extended data Figure 6b and 8*). This seismicity could indicate activation of pre-existing subvertical faults [44] above a deep (> 55 km) depleting reservoir (R1,*4*), as has been observed during caldera collapse events [45]: if so, these faults would be much deeper than documented elsewhere. Analog models for collapse of a caldera with a high-roof aspect ratio (thickness/width >> 1) indicate reverse fault motions during an initial downsag stage [46], in agreement with the focal mechanism of the May 14, 2019 Mw4.9 swarm 1 region earthquake (*Figure 4 and extended data Figure 8*) and [1].

The VLF events located above swarm 1 may be generated by the resonance of a fluid-filled (magma, gas or hydrothermal) shallower cavity or a fluid-filled crack, most probably at the

base of the crust. The characteristic frequency and duration of these events are very different from VLF events typically observed in volcanic zones e.g. [47]. Simple up-scaling of fluid resonance models [48,49] implies a shallower reservoir size of several kilometres (R3, *Figure 4*). The excitation mechanism could be rapid slip and related strain on faults close to the reservoir, or episodic collapse of a piston at the base of this shallow reservoir [47]. The acoustic plumes emanating from the overlying Horseshoe edifice may result from actively degassing of this shallower reservoir.

Both the distribution of seismicity over time and the surface deformation models suggest the drainage of an exceptionally deep reservoir by a dyke that propagated from the base of the brittle lithosphere to the eastern portion of the Mayotte ridge, possibly intersecting another vertical storage zone below seismic swarm 2 before reaching the surface *(R2, Figure 4 and extended data Figure 8)*. Within the uncertainties the GNSS isotropic model may reflect the drainage of reservoir R2 in the brittle lithosphere. The deeper reservoir (R1) may have slowly recharged from the asthenosphere before reaching tensile failure in May 2018 [50].

Magma roots and paths.

The eastern segment of the Mayotte ridge, along which the dike propagated, has the same orientation as many other volcanic features over a range of scales (Quaternary dykes, volcanic vent alignments, ridges and volcanic rift zones) in the northeastern part of Mayotte Island [15] and in and around the other Comoros islands [13,51] (*Figure 5 and extended data Figure 9*). The left-lateral en-echelon arrangement of these features resembles that of extensional tectonic structures in a context of oblique extension (i.e in segmented and diffuse strike-slip fault systems [52] or highly-oblique rifting (e.g. [53,54,55]). We infer that the Mayotte ridge results from the interplay between volcanism and tectonics. The location and orientation of the volcanic features may be in part controlled by the pre-existing Mesozoic fracture zones [6] but they probably also emplace along new tectonic structures. These tectonic structures are extensional (fissures or

step-overs) and open as a result of volcano-tectonic interactions in a wide E-W striking zone, to transfer the strain between the N-S striking offshore branches of the East African rift [56] and the grabens of Madagascar (Aloatra and Ankai) [57]. In this context, high strain rates [54] or highly damaged zones may develop [58] (*Figure 5a inset*) in between the main en-echelon extensional structures. Such zones may constitute high-permeability zones where large magmatic reservoirs can develop. The main Comoros volcanic islands may have grown above such zones.

Between Mayotte and Madagascar, the lithosphere-asthenosphere boundary (LAB) is a sharp limit between a high-velocity 150 Ma lithosphere and a low-velocity asthenosphere, at about 70 km depth [59,60]. The low-velocity asthenosphere is interpreted as hot material spreading beneath the Mascarene basin and beyond [61]. Heating of the base of the oceanic lithosphere damaged by extensional tectonic and loaded by Mayotte island [62] may favour the ponding of large volumes of buoyant melts. Pore pressure increase in these zones may in turn favour failure of deep reservoirs and faults inside the brittle lithosphere

The largest eruption ever documented in submarine domain

The NVE extruded volume (as of May 2019) is 30 to 1000 times larger than that estimated for other deep-sea eruptions [63,25,64,21]. It is difficult to evaluate the dense rock equivalent (DRE) volume [20], but, taking an upper bound of 50% for the DRE factor [65], compatible with the 40% vesicularity of our rock sample [26], the DRE erupted volume could be as large as 2.5 km^3, which is larger than the 1.2 to 1.5 km^3 Havre silicic eruption [66]), previously considered to be the largest documented submarine eruption. It would be 2.5 times larger than the Bardabunga eruption (Iceland's largest eruption of the last two centuries) [43] and only 6 times less than Iceland's 1783-1784 Laki eruption, considered to be one of the largest basaltic eruptions witnessed by humanity [67]. The volumes and flux of emitted lava during the Mayotte magmatic event are comparable to those observed during eruptions at Earth's largest hot spots (Hawaii, Iceland, [43,68] and one quarter of that emplaced yearly over the entire mid-ocean ridge system (mean estimate from

spreading rates over the last 80 Ma [69]). It thus represents a considerable input in terms of CO2 flux [70].

Future scenarios could include a new caldera collapse, submarine eruptions on the upper slope, or onshore eruptions. Large lava flows and cones on the upper slope and onshore Mayotte indicate that this has occurred in the past. Since the discovery of the NVE, an observatory has been established to monitor activity in real time (REVOSIMA [71]) and return cruises continue to follow the evolution of the eruption and edifices.

References

1 Cesca, S. *et al.* Drainage of a deep magma reservoir near Mayotte inferred from seismicity and deformation. *Nat. Geosci.* **13**, 87-93, doi:10.1038/s41561-019-0505-5 (2020).

2 Lemoine, A., Bertil, D., Roullé, A. & Briole, P. The volcano-tectonic crisis of 2018 east of Mayotte, Comoros islands. *Geophys. J. Int.*

3 REVOSIMA, R. d. s. V. e. S. d. M. REVOSIMA (2020), Bulletin n°18 de l'activité sismo-volcanique à Mayotte, du 1 au 31 août, . Report No. 2680-1205, (2020).

4 U.S. Geological Survey. (https://earthquake.usgs.gov/earthquakes/search 2019).

5 Zinke, J., Reijmer, J. & Thomassin, B. Systems tracts sedimentology in the lagoon of Mayotte associated with the Holocene transgression. *Sedimentary Geology* **160**, 57-79 (2003).

6 Phethean, J. J. *et al.* Madagascar's escape from A frica: A high - resolution plate reconstruction for the W estern S omali B asin and implications for supercontinent dispersal. *Geochemistry, Geophysics, Geosystems* **17**, 5036-5055 (2016).

7 Pelleter, A.-A. *et al.* Melilite-bearing lavas in Mayotte (France): An insight into the mantle source below the Comores. *Lithos* **208-209**, 281-297, doi:10.1016/j.lithos.2014.09.012 (2014).

8 Class, C., Goldstein, S. L., Altherr, R. & Bachèlery, P. The process of plume–lithosphere interactions in the ocean basins—the case of Grande Comore. *Journal of Petrology* **39**, 881-903 (1998).

9 Claude-Ivanaj, C., Bourdon, B. & Allègre, C. J. Ra–Th–Sr isotope systematics in Grande Comore Island: a case study of plume–lithosphere interaction. *Earth and Planetary Science Letters* **164**, 99-117 (1998).

10 Ebinger, C. J. & Sleep, N. Cenozoic magmatism throughout east Africa resulting from impact of a single plume. *Nature* **395**, 788-791 (1998).

11 Reiss, M., Long, M. & Creasy, N. Lowermost mantle anisotropy beneath Africa from differential SKS - SKKS shear - wave splitting. *Journal of Geophysical Research: Solid Earth* **124**, 8540-8564 (2019).

12 Class, C., Goldstein, S. L., Stute, M., Kurz, M. D. & Schlosser, P. Grand Comore Island: A well-constrained "low 3He/4He" mantle plume. *Earth and Planetary Science Letters* **233**, 391-409 (2005).

13 Nougier, J., Cantagrel, J. & Karche, J. The Comores archipelago in the western Indian Ocean: volcanology, geochronology and geodynamic setting. *J. Afr. Earth Sci. (1983)* **5**, 135-145 (1986).
14 Michon, L. in *Active volcanoes of the southwest Indian Ocean* (eds P Bachelery, J-F Lénat, A Di Muro, & L Michon) 233-244 (Springer, 2016).
15 Nehlig, P. *et al.* Report French geological map (1/30 000), sheet Mayotte (1179). Orléans: BRGM, 74 p. . **Geological map by Lacquement F., Nehlig P, Bernard J. (2013).** (2013).
16 Audru, J.-C., Guennoc, P., Thinon, I. & Abellard, O. Bathymay : la structure sous-marine de Mayotte révélée par l'imagerie multifaisceaux. *Comptes Rendus Geoscience* **338**, 1240-1249, doi:10.1016/j.crte.2006.07.010 (2006).
17 Sanjuan, B. *et al.* Estimation du potentiel géothermique de Mayotte : Phase 2 - Étape 2. Investigations géologiques, géochimiques et géophysiques complémentaires, synthèse des résultats. 82 (BRGM, Orléans, France, 2008).
18 Feuillet, N. MAYOBS1 French Oceanographic cruise, RV Marion Dufresne. doi:https://doi.org/10.17600/18001217 (2019).
19 SHOM. (2014). Transit valorisé de Mayotte à Brest, https://doi.org/10.17183/S201406900.
20 Rubin, K. H. *et al.* Volcanic eruptions in the deep sea. *Oceanography* **25**, 142-157 (2012).
21 Chadwick Jr, W. W. *et al.* Recent eruptions between 2012-2018 discovered at West Mata submarine volcano (NE Lau Basin, SW Pacific) and characterized by new ship, AUV, and ROV data. *Frontiers in Marine Science* **6**, 495 (2019).
22 Clague, D. A. *et al.* Structure of Lō'ihi Seamount, Hawai'i, and Lava Flow Morphology from High-resolution Mapping. *Frontiers in Earth Science* **7**, 58 (2019).
23 Cole, J., Milner, D. & Spinks, K. Calderas and caldera structures: a review. *Earth-Science Reviews* **69**, 1-26 (2005).
24 Yeo, I. A. & Searle, R. High-resolution Remotely Operated Vehicle (ROV) mapping of a slow-spreading ridge: Mid-Atlantic Ridge 45° N. *Geochemistry, Geophysics, Geosystems* **14**, 1693-1702 (2013).
25 Clague, D. A. *et al.* High-resolution AUV mapping and targeted ROV observations of three historical lava flows at Axial Seamount. *Oceanography* **30**, 82-99 (2017).
26 Bachelery, P. *et al.* Petrological and Geochemical Characterization of the Lava from the 2018-2019 Mayotte Eruption: First Results. *AGUFM* **2019**, V52D-06 (2019).
27 Cathalot, C. *et al.* Acoustic and Geochemical Anomalies in the Water Column around the Newly Formed Volcano offshore Mayotte Island. *AGUFM* **2019**, V52D-05 (2019).
28 Resing, J. A. *et al.* Active submarine eruption of boninite in the northeastern Lau Basin. *Nature Geoscience* **4**, 799-806 (2011).
29 Baumberger, T. *et al.* Understanding a submarine eruption through time series hydrothermal plume sampling of dissolved and particulate constituents: W est M ata, 2008–2012. *Geochemistry, Geophysics, Geosystems* **15**, 4631-4650 (2014).
30 Baker, E. T. *et al.* Hydrothermal discharge during submarine eruptions: The importance of detection, response, and new technology. *Oceanography* **25**, 128-141 (2012).
31 Chadwick, W. W. *et al.* Imaging of CO2 bubble plumes above an erupting submarine volcano, NW Rota-1, Mariana Arc. *Geochemistry, Geophysics, Geosystems* **15**, 4325-4342 (2014).
32 Somoza, L. *et al.* Evolution of submarine eruptive activity during the 2011–2012 E l H ierro event as documented by hydroacoustic images and remotely operated vehicle observations. *Geochemistry, Geophysics, Geosystems* **18**, 3109-3137 (2017).

33 Sohn, R. A. *et al.* Explosive volcanism on the ultraslow-spreading Gakkel ridge, Arctic Ocean. *Nature* **453**, 1236-1238 (2008).

34 Tarantola, A. Linearized inversion of seismic reflection data. *Geophysical prospecting* **32**, 998-1015 (1984).

35 Anderson, E. Dynamics of formation of cone-sheets, ring-dikes, and cauldron subsidences: Royal Society of Edinburgh Proceedings, v. 56. (1936).

36 Nikkhoo, M., Walter, T. R., Lundgren, P. R. & Prats-Iraola, P. Compound dislocation models (CDMs) for volcano deformation analyses. *Geophysical Journal International*, ggw427 (2016).

37 Dofal, A., Fontaine, F. R., Michon, L., Barruol, G. & Tkalcic, H. in *AGU Fall Meeting 2018*. (AGU).

38 Merz, D., Caplan- Auerbach, J. & Thurber, C. Seismicity and Velocity Structure of Lō'ihi Submarine Volcano and Southeastern Hawai'i. *Journal of Geophysical Research: Solid Earth* **124**, 11380-11393 (2019).

39 Wolfe, C., Okubo, P. & Shearer, P. Mantle fault zone beneath Kilauea Volcano, Hawaii. *Science* **300**, 478-480, doi:10.1126/science.1082205 (2003).

40 Ekström, G., Nettles, M. & Dziewoński, A. The global CMT project 2004–2010: Centroid-moment tensors for 13,017 earthquakes. *Physics of the Earth and Planetary Interiors* **200**, 1-9 (2012).

41 Toda, S., Stein, R. & Sagiya, T. Evidence from the AD 2000 Izu islands earthquake swarm that stressing rate governs seismicity. *Nature* **419**, 58-61, doi:10.1038/nature00997 (2002).

42 Ágústsdóttir, T. *et al.* Strike- slip faulting during the 2014 Bárðarbunga- Holuhraun dike intrusion, central Iceland. *Geophysical Research Letters* **43**, 1495-1503 (2016).

43 Sigmundsson, F. *et al.* Segmented lateral dyke growth in a rifting event at Bárðarbunga volcanic system, Iceland. *Nature* **517**, 191-195, doi:10.1038/nature14111 (2015).

44 Jacques, E. *et al.* in *AGU* (Online everywhere, 2020).

45 Gudmundsson, M. T. *et al.* Gradual caldera collapse at Bárdarbunga volcano, Iceland, regulated by lateral magma outflow. *Science* **353**, aaf8988 (2016).

46 Roche, O., Druitt, T. & Merle, O. Experimental study of caldera formation. *Journal of Geophysical Research: Solid Earth* **105**, 395-416 (2000).

47 Kumagai, H. *et al.* Very-Long-Period Seismic Signals and Caldera Formation at Miyake Island, Japan. *Science* **293**, 687-690, doi:10.1126/science.1062136 (2001).

48 Fazio, M., Alparone, S., Benson, P. M., Cannata, A. & Vinciguerra, S. Genesis and mechanisms controlling tornillo seismo-volcanic events in volcanic areas. *Scientific reports* **9**, 1-11 (2019).

49 Maeda, Y. & Kumagai, H. A generalized equation for the resonance frequencies of a fluid-filled crack. *Geophysical Journal International* **209**, 192-201 (2017).

50 Sigmundsson, F. *et al.* Unexpected large eruptions from buoyant magma bodies within viscoelastic crust. *Nature Communications* **11**, 1-11 (2020).

51 Famin, V., Michon, L. & Bourhane, A. The Comoros archipelago: a right-lateral transform boundary between the Somalia and Lwandle plates. *Tectonophysics* **789**, 228539 (2020).

52 Armijo, R., Meyer, B., Navarro, S., King, G. & Barka, A. Asymmetric slip partitioning in the Sea of Marmara pull- apart: A clue to propagation processes of the North Anatolian fault? *Terra Nova* **14**, 80-86 (2002).

53 Dauteuil, O. & Brun, J.-P. Oblique rifting in a slow-spreading ridge. *Nature* **361**, 145-148 (1993).

54 Brune, S. Evolution of stress and fault patterns in oblique rift systems: 3-D numerical lithospheric-scale experiments from rift to breakup. *Geochemistry, Geophysics, Geosystems* **15**, 3392-3415 (2014).

55 Pagli, C., Yun, S.-H., Ebinger, C., Keir, D. & Wang, H. Strike-slip tectonics during rift linkage. *Geology* **47**, 31-34 (2019).

56 Franke, D. *et al.* The offshore East African Rift System: Structural framework at the toe of a juvenile rift. *Tectonics* **34**, 2086-2104 (2015).

57 Rufer, D., Preusser, F., Schreurs, G., Gnos, E. & Berger, A. Late Quaternary history of the Vakinankaratra volcanic field (central Madagascar): insights from luminescence dating of phreatomagmatic eruption deposits. *Bulletin of volcanology* **76**, 817 (2014).

58 Peacock, D. & Anderson, M. THE SCALING OF PULL-APARTS AND IMPLICATIONS FOR FLUID FLOW IN AREAS WITH STRIKE-SLIP FAULTS. *Journal of Petroleum Geology* **35**, 389-399 (2012).

59 Pratt, M. J. *et al.* Shear velocity structure of the crust and upper mantle of Madagascar derived from surface wave tomography. *Earth and Planetary Science Letters* **458**, 405-417 (2017).

60 Mazzullo, A. *et al.* Anisotropic Tomography Around La Réunion Island From Rayleigh Waves. *J. Geophys. Res. Solid Earth* **122**, 9132-9148, doi:10.1002/2017JB014354 (2017).

61 Barruol, G. *et al.* Large-scale flow of Indian Ocean asthenosphere driven by Réunion plume. *Nat. Geosci.* **12**, 1043-1049, doi:10.1038/s41561-019-0479-3 (2019).

62 Zhong, S. & Watts, A. Lithospheric deformation induced by loading of the Hawaiian Islands and its implications for mantle rheology. *Journal of Geophysical Research: Solid Earth* **118**, 6025-6048 (2013).

63 Watts, A. B. *et al.* Rapid rates of growth and collapse of Monowai submarine volcano in the Kermadec Arc. *Nature Geosci* **5**, 510-515, doi:10.1038/ngeo1473 (2012).

64 Chadwick Jr, W. W. *et al.* A recent volcanic eruption discovered on the central Mariana back-arc spreading center. *Frontiers in Earth Science* **6**, 172 (2018).

65 Schipper, C. I., White, J. D., Houghton, B., Shimizu, N. & Stewart, R. B. Explosive submarine eruptions driven by volatile-coupled degassing at Lōihi Seamount, Hawaii. *Earth and Planetary Science Letters* **295**, 497-510 (2010).

66 Carey, R. *et al.* The largest deep-ocean silicic volcanic eruption of the past century. *Science advances* **4**, e1701121 (2018).

67 Thordarson, T. & Self, S. The Laki (Skaftár Fires) and Grímsvötn eruptions in 1783-1785 *Bull Volcanol* **55**, 233-263 (1993).

68 Neal, C. *et al.* The 2018 rift eruption and summit collapse of Kīlauea Volcano. *Science* **363**, 367-374 (2019).

69 Cogné, J.-P. & Humler, E. Temporal variation of oceanic spreading and crustal production rates during the last 180 My. *Earth and Planetary Science Letters* **227**, 427-439 (2004).

70 Marty, B. & Tolstikhin, I. N. CO2 fluxes from mid-ocean ridges, arcs and plumes. *Chemical Geology* **145**, 233-248 (1998).

71 REVOSIMA, R. d. s. V. e. S. d. M. Bulletin n°16 de l'activité sismo-volcanique à Mayotte, du 1 au 31 mars 2020. (2020).

72 Debeuf, D. *Étude de l'évolution volcano-structurale et magmatique de Mayotte, Archipel des Comores, océan Indien: approches structurale, pétrographique, géochimique et géochronologique*, (2009).

73 Stamps, D., Saria, E. & Kreemer, C. A Geodetic Strain Rate Model for the East African Rift System. *Sci, Rep,* **8**, 732, doi:10.1038/s41598-017-19097-w (2018).
74 Deville, E. *et al.* Active fault system across the oceanic lithosphere of the Mozambique Channel: implications for the Nubia–Somalia southern plate boundary. *Earth and Planetary Science Letters* **502**, 210-220 (2018).
75 Macgregor, D. History of the development of the East African Rift System: A series of interpreted maps through time. Journal of African Earth Sciences 101, 232-252 (2015).

Correspondence and requests for materials should be addressed to Nathalie Feuillet (feuillet@ipgp.fr)

Author Information

Océane Foix

Present address : Montpellier 2 University, France

Manuel Moreira

Present address: Orleans University, France

Affiliations

Université de Paris, Institut de physique du globe de Paris, CNRS, F-75005 Paris, France

Nathalie Feuillet, Wayne C. Crawford, Christine Deplus, , Eric Jacques, Jean Marie Saurel, Claudio Satriano, Océane Foix, Philippe Kowalski, Angèle Laurent, Manuel Moreira, Aline Peltier, François Beauducel, Raphaël Grandin, , Romuald Daniel, Jérémy Gomez, Simon Besançon, Pascal Bernard, Arnaud Lemarchand

IFREMER, Unité Géosciences Marines, Technopole La Pointe du Diable, 29280 Plouzané, France

Stephan. Jorry, Chastity Aiken, Emmanuel Rinnert, Cécile Cathalot, Jean-Pierre Donval, Vivien Guyader, Arnaud Gaillot, Carla Scalabrin, Pascal Pelleau, Louis Geli, Yves Fouquet,

Bureau de Recherches Géologiques et Minières - BRGM, DGR/GBS, F-45060 Orléans, France
Isabelle Thinon, Anne Lemoine, Fabien Paquet, Didier Bertil

LIttoral ENvironnement et Sociétés (LIENSs) UMR7266, Université de La Rochelle - CNRS, 2 rue Olympe de Gouges, 17000 La Rochelle

Valerie Ballu

Université Clermont Auvergne, CNRS, IRD, OPGC, Laboratoire Magmas et Volcans, F-63000 Clermont-Ferrand, France,

Patrick Bachelery

Institut de Physique du Globe de Strasbourg UMR7516 CNRS Université de Strasbourg, 5 rue René Descartes 67000 Strasbourg, France

Jérôme Van der Woerd

Acknowledgements

We thank captain A. Eyssautier and the officers and the crew of the R/V *Marion Dufresne* (TAAF/IFREMER/LDA), GENAVIR's coordinator, M. Boudou D'hautefeuille, and the shipboard operations engineers. We thank the captain and crew of the M/V *Ylang* (SGTM company). This research was supported by the French Ministries of Environment, Research and Overseas under a research project to N.F. (proposal INSU-CT3 TELLUS SISMAYOTTE 2019). The french national geographic Institute (IGN) provided the Mayotte GNSS data. The la Réunion university (Laboratory of atmosphere and hurricanes) provided data from the DSUA station in Madagascar (contract INTERREG-5 Indian Ocean 2014-2020 "ReNovRisk-Cyclones").

We thank CNRS/INSU, IPGP, IFREMER, BRGM for additional support under internal funds. We thank our colleagues F. Tronel, A. Roulle, E. Dectot, A. Colombain, C. Doubre, Daniel Sauter, Antony Dofal and Antoine Villié for assistance in the field, previous data acquisition,

processing and model development. We thank Olivier Desprez de Gesincourt, L. Testut and T. Tranchant for loan and data processing of the seafloor pressure sensors. We thank the French National Marine Hydrographic and Oceanographic Service (SHOM) for providing us with previous data from the area. We thank G. Barruol for discussions. This is IPGP contribution number XXXX.

Author contributions

NF, SJ, WCC, CD, IT, EJ, JMS, ALe, FP, RD, AG, CA, OF, PK, ALa, JPD, LG, JG, VG, PP, ER participated on the MAYOBS1 cruise (NF, SJ and WCC as PI), acquired and processed the geophysical and seismological data. CSa, ALa and PB detected and located the VLF events. AP was in charge of the GNSS installation in Glorieuse island and processed and modeled the GNSS data with FB and RG. VB was in charge of the OBSs APGs and processed their data. SB participated in the first OBS deployment on the Ylang vessel with WC and RD. DB, ALM and JVW were responsible for the installation of new seismological and GNSS stations in Mayotte and of data acquisition onshore. JPD, VG, ER, CC performed the geochemical analysis and interpretation of the water column data. CSc and AG processed the EM122 acoustic data. CD and AG performed the depth changes calculation. CSc provided the interpretation of the water column acoustic data. PBa and YF furnished the rocks sample descriptions and petrological analysis. NF, SJ, CD, PBa, YF, IT, FP, JVW, EJ provided the geological interpretation. NF wrote the paper with the contribution of all other authors. P.B. JMS, EJ, WCC, CSa, PB, ALe, GL, CA, VB, AG, AP, FB, RG, ER, CC, CSc wrote the method section and the supplementary material.

Competing interests

The authors declare no competing interests.

FIGURE CAPTIONS

Figure 1: The volcanic ridge offshore Mayotte. a) 3D Westward view of Mayotte island and insular slope (vertical exaggeration 3). Green stars: Acoustically-detected plumes above the Horseshoe, the NVE and the degassing area on Petite-Terre island. Left inset: geographic setting and Global Navigation Satellite System (GNSS) surface horizontal displacements stations. Black points: seismic stations. Dashed grey lines: Mesozoic fracture zones [6]. b) Geological interpretations of MAYOBS1 data. Purple patches: Volcanic structures (mainly cones). Pink patches: lava flows and elongated features. Yellow patches: upper slope's high reflective lava flows. NVE: in red (central part) and orange (radial ridges and flat flows). Green stars as in a). Red lines: fissures and faults, dashed lines: inferred faults. black dots: bathymetric depression. White boxes: location of Fig.2a and Extended data Fig. 3. Inset, as in b with MAYOBS backscatter data. Pink dots: Ocean Bottom seismometer (OBS) seismicity: yellow diamonds: location of the Very Low Frequency earthquakes. White boxes: location of extended data Figure 3.

Figure 2: The new volcanic edifice (NVE) offshore Mayotte. a) 30 m resolution bathymetric maps from shipboard EM122 multibeam, illuminated from N290°E. upper panel: SHOM bathymetry collected in 2014 [19]. lower panel: MAYOBS1 bathymetry collected in May 2019 [18]. black circle: position of dredge DR01. b) Depth changes between 2014 and 2019. The change in topography is estimated to be significant when larger than 10 m.

Figure 3: The new volcanic edifice (NVE) and the acoustic plume. a) Southward 3D view of the NVE and the water column acoustic plume observed one hour before the Conductivity-Temperature-Depth (CTD) rosette on May 16th 2019. The White dot and blue patch indicate the position of the CTD rosette deployment, 1 km far from the summit the volcano. Right inset: Processed polar echogram from one EM122 multibeam ping on May 16th (13:33 UT), horizontal and vertical-axes (both in meters) correspond respectively to the cross-track distance and the water depth.

Figure 4: Conceptual model of the submarine eruption offshore Mayotte eruption. Bathymetry as in Figure 1b, no vertical exaggeration. Purple zones: N130°E volcano-tectonic ridges and segments. Dashed white lines: inferred ancient caldera with degassing zones above. Cross-section: red and reddish zones: magma storage zones (mush or magma chambers) and magma pathways involved in the 2018-2020 Mayotte volcanic crisis and seafloor eruption. Yellow layer: sediments. Dashed lines: subvertical faults beneath inferred caldera possibly reactivated by the deflation of a deep reservoir. White arrow: possible downsag at an initial stage of caldera collapse. Pink dots: 800 earthquakes located using OBSs and land stations. Other dots: 139 earthquakes from before the OBS deployment: colored dots are from the first 6 weeks of the crisis and white dots from the remaining 8 months before the OBS deployment. Yellow diamonds: Very Low Frequency (VLF) earthquakes. Blue and red triangles: water and magma movements, respectively. Blue patch: Location, with 3 sigma uncertainties, of the most robust isotropic source deformation model. Moho depth from [37]. Lithosphere/asthenosphere boundary depth from [60,61].

Figure 5: Regional volcano-tectonic setting of the submarine eruption offshore Mayotte. a) Volcano-tectonic setting of the new volcanic edifice (NVE). Volcanic cones and ridges (purple) from this study and [13,72,16,51]. Dots and diamonds : earthquakes as in Figure 4 and Extended data Fig. 6 and 8. Focal mechanisms for M>5 earthquakes [40]. Dotted white arrow: dyking intrusion along eastern segment of the Mayotte volcanic ridge. Red ellipse: inferred main volcano-tectonic ridges. Purple ellipses: highly damaged zones in between the en echelon ridges. Thick black arrows: local extension direction. Inset: sandbox model adapted from [58] illustrating the possible arrangement of the main volcano-tectonic structures in Comoros. b) Geodynamic setting of the East African Rift systems. Main tectonic structures and extensional zones in Africa and Madagascar from this study and [73,57,74,75,56]. Purple patches: Quaternary volcanism in Madagascar [57]. Red dots: M> 2.5 earthquakes [4] with focal mechanisms from [40] for the M>5 earthquakes. Arrows: GNSS horizontal motions [73]. Small purple ellipses in the Comoros as in a) with double dark red arrows: the volcanic ridge east of Mayotte and extension direction. Inset: Simplified tectonic map of the East African Rift system: Yellow highlights: most active rifts and graben; Red ellipse: Transfer zone of the Comoros with direction of lateral motion.

METHODS

Summary

Ship-borne Multibeam data was acquired using a Kongsberg EM122 1°x1° during the 2014 [19] and 2019 [18]. **Ship-borne Multibeam data** were processed with the GLOBE software [76] to provide 30-m grid spaced digital terrain models and seafloor backscatter imagery and to calculate depth differences, surface and volumes. The 3D acoustic water column data from the 2019 cruise were processed using SonarScope (@Ifremer) and GLOBE softwares https://doi.org/10.17882/70460 [76]. **Water column measurements:** A CTD-Rosette Seabird 911+ CTD (Conductivity; Temperature; Depth) equipped with an altimeter, an Aanderaa oxygen optode and a Seapoint Turbidity Meter was mounted on a carousel with 16 ®Niskin sampling bottles (8L) to measure and sample throughout the water column. Sub-sampling was performed for onboard analyses (pH, alkalinity and total CO2 by pH electrode and titrator) and for onshore analyses (CH4 analysis by the purge and trap method and H2 and CO2 analysis by the Headspace method). **Seismology:** 800 earthquakes identified from the onshore catalog were selected in descending magnitude order and manually picked onboard. The seismic network used during the two month deployment included OBSs, onshore local and regional stations (up to 500km distance). The events were relocated with NonLinLoc [77] and an hybrid velocity model based on trials with 6 different velocity models, achieving final location accuracies better than 5km. Eighty-four very low frequency (VLF) earthquakes were detected between February 25 and April 24, 2019, using an amplitude trigger on ocean bottom hydrophones recordings, filtered between 0.05 and 0.10 Hz, followed by a selection of events with a clear peak frequency and a final visual inspection. VLF earthquakes were located using spatial 3D back-projection of station-pair cross-correlation functions [78], assuming a constant surface-wave speed of 3.5 km/s. A well-constrained epicentral location was obtained for 81 events. **Geodesy:** We inverted the surface deformation recorded by 6 permanent GNSS (Global Navigation Satellite System)

receivers installed in Mayotte, Grande Glorieuse and Madagascar. We used both an isotropic model and a triple volumetric discontinuities (pCDM source) in a homogeneous elastic half-space, isotropic material with Poisson's ratio of 0.25 to model the pressure source in depth. Seafloor pressure data (30s sample interval) were pre-processed using harmonic analysis to remove the tides and low-pass filtering to remove residual oscillations interpreted as internal waves.

Water Column: Bathymetry and water column acoustic data.

See also Extended Data Figures 1 to 3 and Figure 5

We mapped the submarine slope and basin adjacent to Mayotte and detected and mapped water column anomalies using ship-borne multibeam surveys over an area of 8600 km^2. Bathymetric data were collected in 2014 by the French *Service Hydrographique et Océanographique de la Marine* [19] using the vessel BHO Beautemps Beaupré. The 2019 data [18] were collected using the R/V Marion Dufresne during the MAYOBS1 cruise (May 3rd to 18th). Both vessels are equipped with identical Kongsberg EM122 multibeam echosounders (12 kHz, 1°x1° beam width). Bathymetry and seafloor backscatter data sets were processed using the GLOBE software [76] with identical 30-m cell grids to allow accurate estimates of differences in depth, surfaces and volumes. Water column acoustic data are only available for the 2019 cruise and processing was performed onboard using the SonarScope (@Ifremer) and GLOBE software packages using published methods [79].

Water column: Sampling and chemical analysis

See also Extended Data Figure 4.

Water column sampling and in situ measurements with CTD-Rosette.

Seawater was sampled using IFREMER's CTD-Rosette, consisting of a Seabird 911+ CTD

683 (Conductivity; Temperature; Depth) instrument mounted on a carousel with 16 8-liter ®Niskin
684 sampling bottles. For this cruise, the CTD-Rosette was equipped with an altimeter, an Aanderaa
685 oxygen optode and a Seapoint turbidity meter. Information from the sensors was transmitted in
686 real time, allowing us to adapt the sampling strategy to observed water column anomalies.
687 The ®Niskin bottles were subsampled for onboard and onshore analyses. For CH_4 analysis,
688 125mL glass bulbs were used for analysis using the purge and trap method. The bulbs were
689 allowed to overflow by at least two volumes of seawater and particular care was taken to
690 exclude air bubbles to prevent contamination. While filling, sodium azide was added to prevent
691 future microbial activity. For H_2 and CO_2 analysis, 160 mL vials were filled using the
692 Headspace method. The vials, containing some sodium azide, were filled using a silicone tube
693 connected to the ®Niskin bottle. The silicone tube was inserted to the bottom of the vial in order
694 to completely fill the vial from the bottom to the top, displacing all contained air. The tube was
695 then slowly removed, taking care to avoid any air bubble, and the vial was sealed with a PTFE
696 septum using special crimping pliers. The headspace volume of 10 mL of atmospheric air was
697 added using a needle mounted on a syringe.
698
699 ***CH_4 analysis by the purge and trap method at IFREMER laboratories.***
700 Onshore, the Purge and trap method [80] was used. Once in the laboratory, CH_4 was stripped from
701 seawater using Helium carrier gas, trapped on activated charcoal at -80°C and detected and
702 quantified with a flame ionization detector after separation on a packed column. Calibration
703 was performed injecting of a commercial gas standard (CH_4 107.8ppm). The limit of detection
704 is 0.03nmol/L, the precision (based on five replicates from the same rosette bottle) is within ±
705 2% (confidence level 95%) and the accuracy is 5%. The CH_4 equipment was set up in a portable
706 clean air-conditioned container, allowing one CH_4 analysis every 6 min using two extraction
707 kits.

CO_2 and H_2 analysis were performed at IFREMER laboratories by GC/HID following methods described in [81], except that the headspace vial replaced the syringe.

pH, Total Alkalinity and ΣCO_2 measurements onboard.

pH, Total Alkalinity and ΣCO_2 measurements were performed onboard using a Metrohm 848 Titrino Plus titrator. The pH electrode was calibrated using commercially available pH buffers. pH was measured as soon as possible after sample recovery and Total Alkalinity and ΣCO_2 were then determined by direct titration with 0.1N hydrochloric acid. Concentrations were compared to a seawater reference for oceanic CO_2 measurements (Batch 178).

Seismology data

See also Supplementary information and Extended Data Figures 6 and 8

The 800 earthquakes discussed in this paper were located using recordings from a network of up to 22 seismological stations equipped with sensors of different types, operating during different time slots comprised between February 25th and May 5th 2019: 6 ocean bottom seismometers (OBS) and up to 16 land stations on Mayotte island, on Grande Glorieuse, on Khartala volcano, in Madagascar and in Kenya. Details on station location, type and quality are provided in Supplementary Information Figures S2.1 and S2.2 and Table S2.1.

An earthquake catalog of 2362 events of magnitude 2.0<M<5.4, between February 25th and May 5th, was produced in near real-time by BRGM using land stations [82]. On board, three groups of operators working around the clock manually picked 800 of the events from the OBS, selected in descending magnitude order, using SeisComP3 software [83]. The Hypo71 software [84] was used for preliminary locations and SeisComP3 was used to compute ML and MLv magnitudes, the velocity model was updated to fit the data (see Supplementary S2) then the NonLinLoc (NLL) software [77] was used to relocate the events. Low-frequency events were

detected and analysed using the broadband land stations and the broadband hydrophone (HiTech HTI-90U, 30s cut-off frequency) on the OBSs.

Geodesy data

See Supplementary Material and Extended Data Figures 7

We used the GNSS stations from the Centre National d'Etudes Spatiales (MAYG), EXAGONE's TERIA network (BDRL and GAMO), Precision Topo's Lel@ network (KAWE), IPGP (GLOR) and the Université de la Réunion (DSUA). Sea floor pressure data were collected using Seabird SBE37 pressure sensors deployed on the OBS frames. The seawater pump of each instrument was deactivated to avoid induced noise on the seismometer recordings. Although SBE37s are not designed for seafloor geodesy, previous experiments indicate that their pressure gauge can be used to characterize sudden or large-amplitude deformations [85,86].

Data availability statement

Data availability statement

The authors declare that most of the data supporting the findings of this study are available within the paper and its supplementary information files. GNSS data are available on the website « http://mayotte.gnss.fr » and can be downloaded on this ftp site ftp://rgpdata.ign.fr/pub/gnss_mayotte/. Ship-borne geophysical data from the MAYOBS1 cruise can be obtained through the French national oceanographic data center SISMER (http://en.data.ifremer.fr/SISMER, doi: https://doi.org/10.17600/18001217) but restrictions apply to the availability of these data. The compilations of older bathymetric and topographic data are available on the SHOM Website (http://www.shom.fr,

https://doi.org/10.17183/S201406900) Rock samples are referenced at https://wwz.ifremer.fr/echantillons/Echantillons/Carte#/map (https://campagnes.flotteoceanographique.fr/prl?id=BFBGX-134187). Samples are accessible on site at IFREMER, Plouzané, France.

Map were created using Globe software https://doi.org/10.17882/70460 [76], ArcGIS® software by Esri (https://www.arcgis.com/index.html), Generic Mapping Tools [87], Adobe illustrator ® (https://www.adobe.com/) and MATLAB.

In addition to Mayobs 1 cruise multibeam data (resolution: 30m) [18], Figs. 1, 2, 4, 5 and Extended data Fig. 1, 2, 3, 6, 7, 8, 9 include topographic and bathymetric data from previous compilation [16,88,90] (https://doi.org/10.17600/14000900, https://doi.org/10.17183) the General Bathymetric Chart of the0 Oceans (https://www.gebco.net) and Global topography from SRTM GL1 (https://catalog.data.gov/dataset/shuttle-radar-topography-mission-srtm-gl1-global-30m). Litto3D Mayotte (https://diffusion.shom.fr/presentation/litto3d-mayot2012.html). Topography and bathymetry of Figure 5b from GeoMapApp (www.geomapapp.org) / CC BY. In Fig 5 and Extended data Figs.6, 8, 9: focal mechanisms for M>5 earthquakes are from [40]. In Figure 5, M> 2.5 earthquakes are from [4]

Code Availability

Ship-borne Multibeam data were processed with the GLOBE software [76]. The 3D acoustic water column data were processed using SonarScope (@Ifremer) and GLOBE softwares https://doi.org/10.17882/70460 [76]. GNSS solutions were computed using the GipsyX/JPL software available at https://gipsy-oasis.jpl.nasa.gov. Deformation source modeling codes (Mogi and Nikkhoo) are available at https://github.com/IPGP/deformations-matlab and data processing has been achieved using the WebObs open-source system available at https://ipgp.github.io/webobs/.

Pressure gauge data were processed with Python [91]. Very Low Frequency Event analysis has been performed using ObsPy [89] NumPy [92] and Matplotlib [93]. Earthquake phase picking was performed with SeisComP3 [94] and initial locations used Hypo71 [84] Final locations were performed with NonLinLoc [77] and results converted back to SeisComP3 using ObsPy [89].

Method References

76 Globe (GLobal Oceanographic Bathymetry Explorer) Software. (2020).

77 Lomax, A., Michelini, A. & Curtis, A. Earthquake location, direct, global-search methods. *Encyclopedia of complexity and system science* **5**, 1-33 (2009).

78 Poiata, N., Satriano, C., Vilotte, J.-P., Bernard, P. & Obara, K. Multiband array detection and location of seismic sources recorded by dense seismic networks. *Geophysical Journal International* **205**, 1548-1573 (2016).

79 Dupré, S. *et al.* Tectonic and sedimentary controls on widespread gas emissions in the Sea of Marmara: Results from systematic, shipborne multibeam echo sounder water column imaging. *Journal of Geophysical Research: Solid Earth* **120**, 2891-2912 (2015).

80 Charlou, J. L., Dmitriev, L., Bougault, H. & Needham, H. D. Hydrothermal CH4 between 12 N and 15 N over the Mid-Atlantic Ridge. *Deep Sea Research Part A. Oceanographic Research Papers* **35**, 121-131 (1988).

81 Donval, J.-P. & Guyader, V. Analysis of hydrogen and methane in seawater by "Headspace" method: Determination at trace level with an automatic headspace sampler. *Talanta* **162**, 408-414 (2017).

82 Bertil.D, Lemoine.A, Colombain.A, Maisonhaute.E & Dectot.G. (BRGM, Orléans, France, 2018).

83 Hanka, W. *et al.* Real-time earthquake monitoring for tsunami warning in the Indian Ocean and beyond. *Natural Hazards & Earth System Sciences* **10** (2010).

84 Lee, W. H. K. & Lahr, J. C. *HYPO71: A computer program for determining hypocenter, magnitude, and first motion pattern of local earthquakes.* (US Department of the Interior, Geological Survey, National Center for …, 1972).

85 Vilaseca, G. *et al.* Oceanographic Signatures and Pressure Monitoring of Seafloor Vertical Deformation in Near-coastal, Shallow Water Areas: A Case Study from Santorini Caldera. *Marine Geodesy* **39**, 401-421 (2016).

86 Fox, C. G. In situ ground deformation measurements from the summit of Axial Volcano during the 1998 volcanic episode. *Geophysical Research Letters* **26**, 3437-3440 (1999).

87 Wessel, P. & Smith, W. H. New, improved version of Generic Mapping Tools released. *Eos, Transactions American Geophysical Union* **79**, 579-579 (1998).

88 SHOM. 2016, MNT bathymétrique de la façade de Mayotte (Homonim), MNT_MAY100m_HOMONIM_WGS84, 2016, https://doi.org/10.17183

89 Krischer, L. *et al.* ObsPy: A bridge for seismology into the scientific Python ecosystem. *Computational Science & Discovery* **8**, 014003 (2015).

90 JORRY, S.(2014). PTOLEMEE cruise, RV L'Atalante, https://doi.org/10.17600/14000900

91 Van Rossum, G. & Drake, F. L. *Python reference manual*. (iUniverse Indiana, 2000).

92 Harris, C. R. *et al.* Array programming with NumPy. *Nature* **585**, 357-362 (2020).

93 Hunter, J. D. Matplotlib: A 2D graphics environment. *IEEE Annals of the History of Computing* **9**, 90-95 (2007).

94 Weber, B. *et al.* in *Geophysical Research Abstracts.*

Paper published in Nature Geoscience , https://doi.org/10.1038/s41561-021-00809-x, Free-to-read: https://rdcu.be/cwd2Z

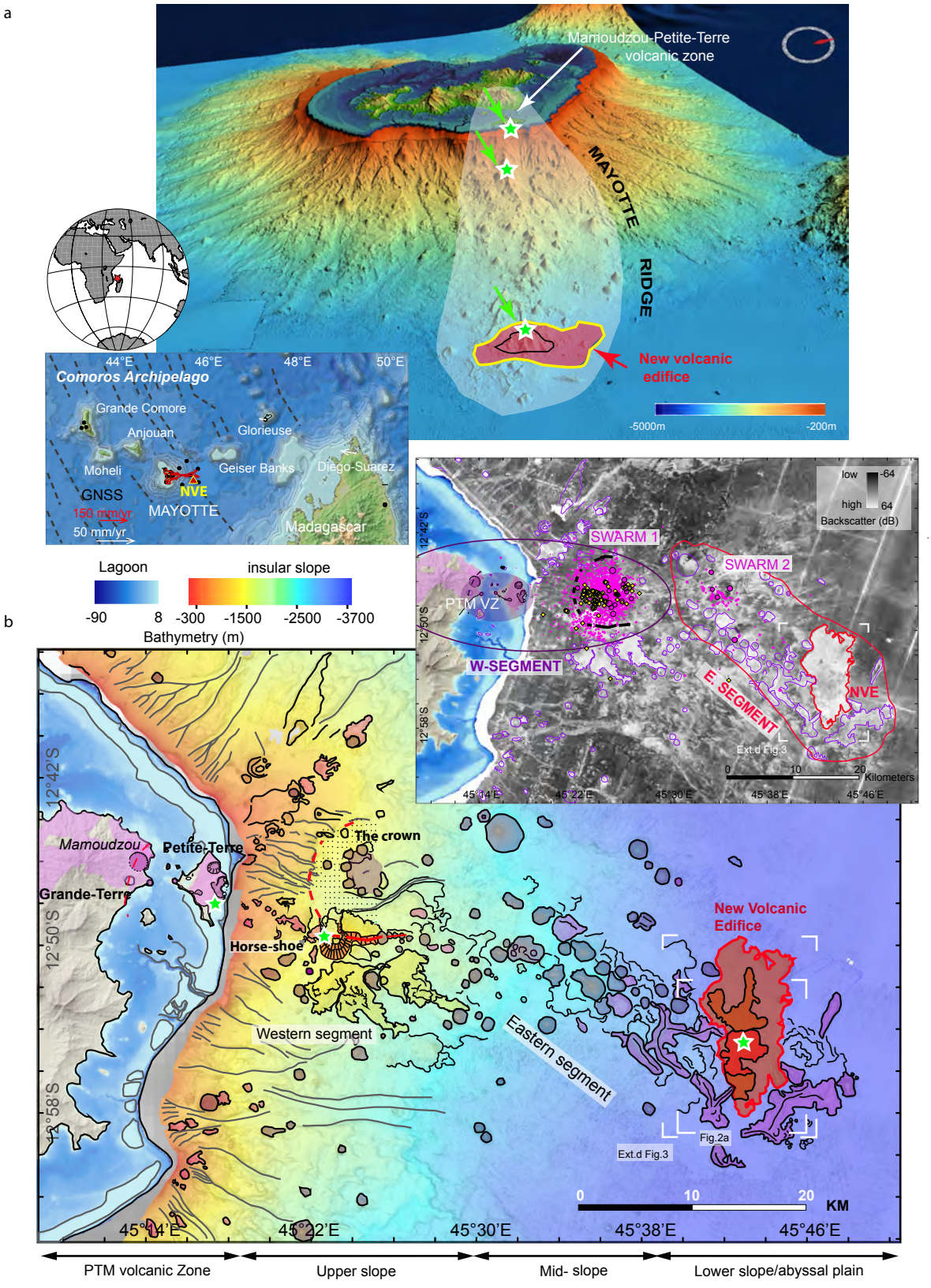

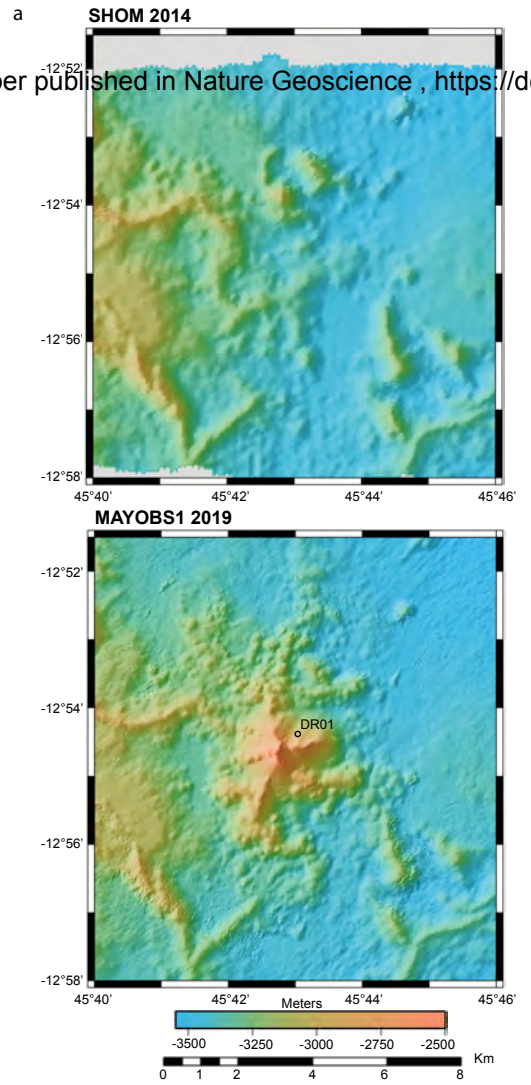

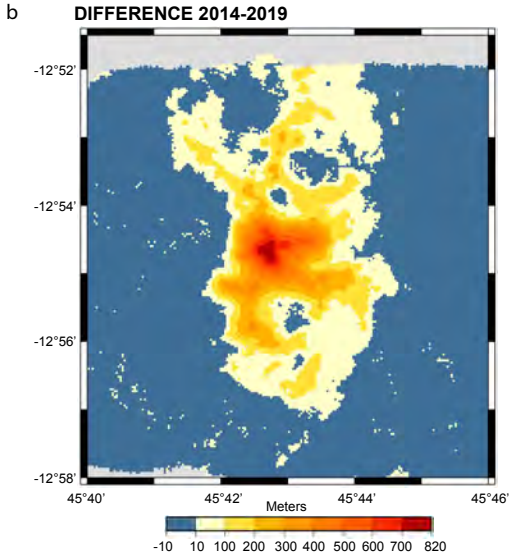

Paper published in Nature Geoscience , https://doi.org/10.1038/s41561-021-00809-x, Free-to-read: https://rdcu.be/cwd2Z

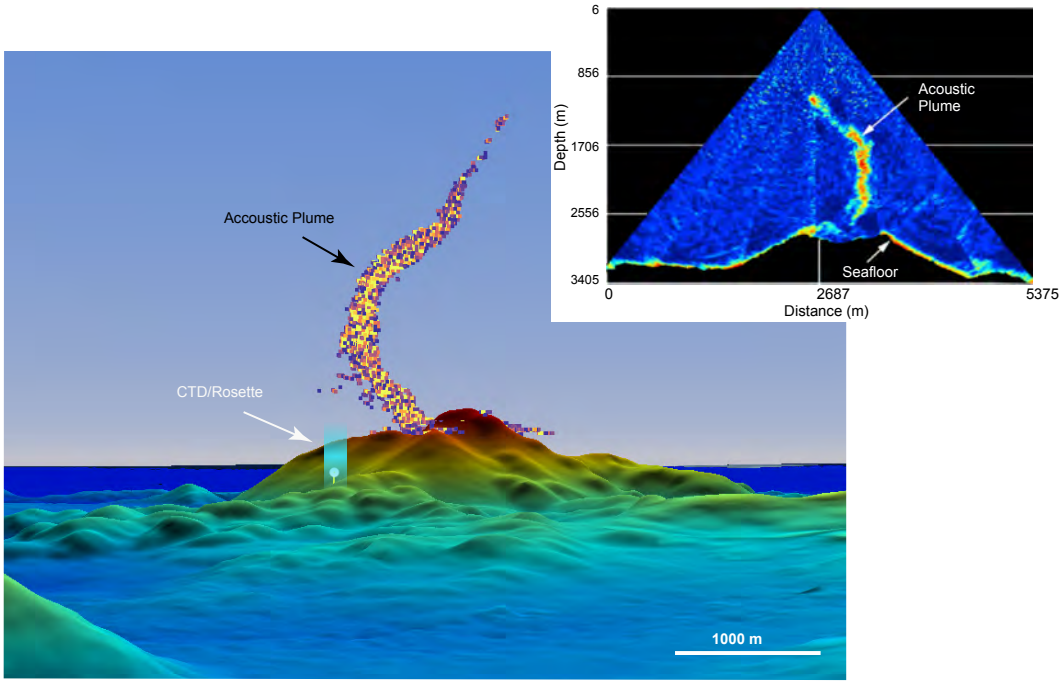

Paper published in Nature Geoscience , https://doi.org/10.1038/s41561-021-00809-x, Free-to-read: https://rdcu.be/cwd2Z

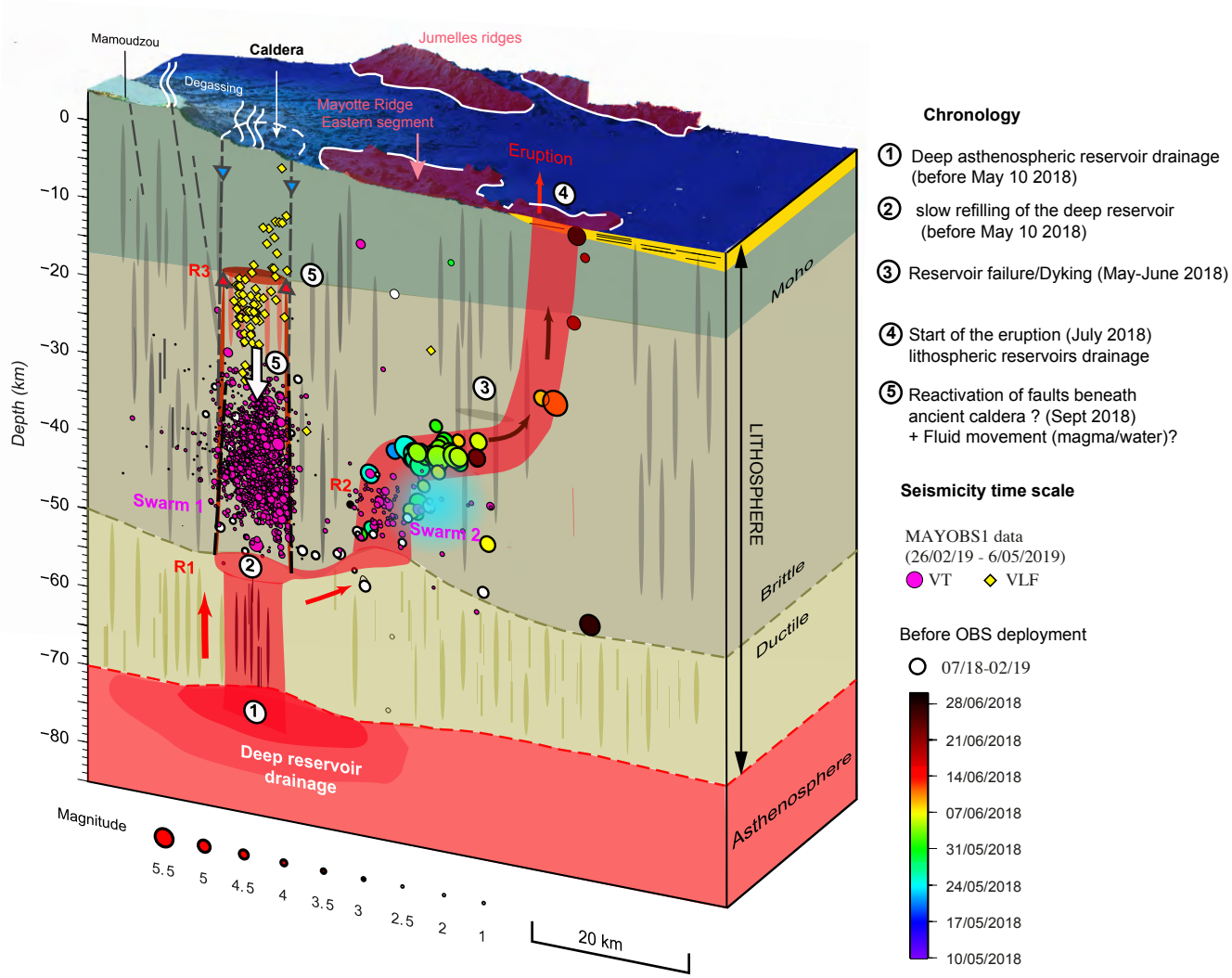

a

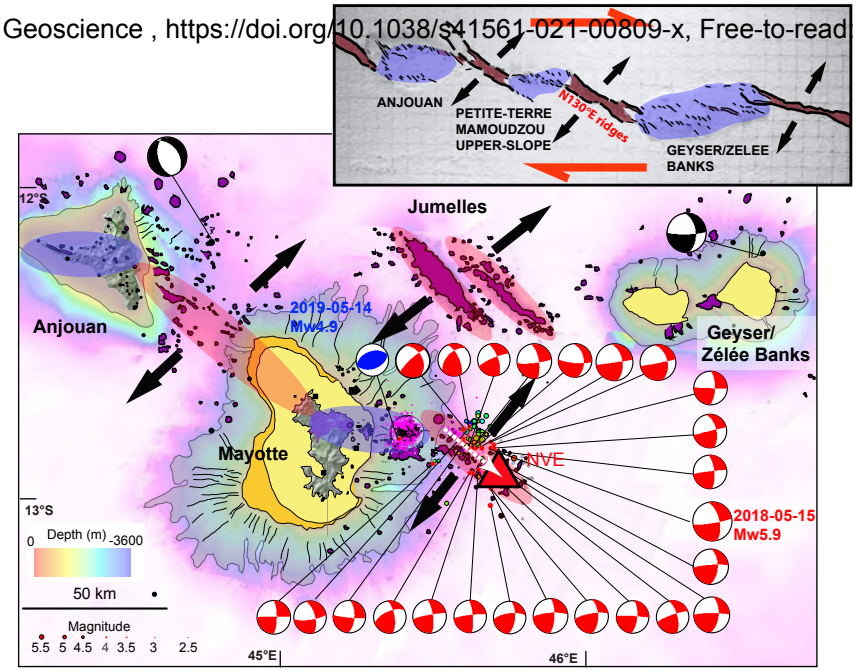

b

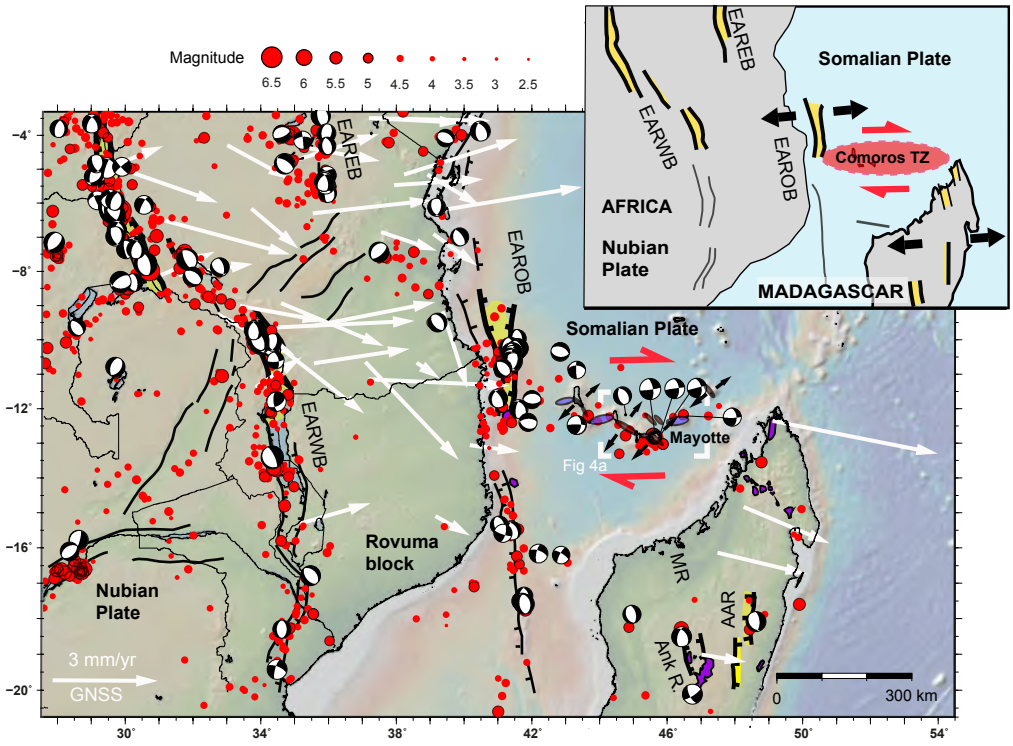

Paper published in Nature Geoscience , https://doi.org/10.1038/s41561-021-00809-x, Free-to-read: https://rdcu.be/cwd2Z

Extended data. Figure 1: **The Mayotte Ridge**. 3-D westward view of submarine volcanic features located east of Mayotte, 3x vertical exaggeration. Bathymetry from MAYOBS1 30-m resolution DTM and [16,88] a) bathymetry (b) Backscatter seafloor reflectivity (white is highest reflectivity) from MAYOBS1 cruise .

Extended data. Figure 2: Volcanic features offshore Mayotte. a) 30-m resolution EM122 multibeam bathymetry (MAYOBS 1 cruise) and [16,88] with locations of Fig 2. b,c,d indicated. b), c) Interpreted MAYOBS1 shipboard bathymetry and backscatter of the upper slope east of Mayotte (location in a). Cones, lava flows and canyons as in Figure 1b. Black dots: bathymetric depression. Dashed red lines: pre-existing caldera structure. d) Interpreted bathymetry of the lower slope east of Mayotte (localisation in a). e) zoom on d) showing monogenetic cones and lava flows.

Extended data. Figure 3: **The new volcanic edifice**. a) 2014 EM122 multibeam seafloor backscatter [19]. b) 2019 reflectivity (MAYOBS 1 cruise) [18]. c) Depth changes between the 2014 and 2019 surveys, superimposed on 2019 reflectivity. The white areas of the 2019 backscatter map exceeding the bathymetric difference map indicate the extent of new volcanic material.

Extended data. Figure 4: **CTD (conductivity temperature-depth)-Rosette measurements**. a) Nephelometry and b) temperature vertical profiles. c)-g) sample analyses from 8L ®Niskin bottles. c)-e) Gas concentrations(CH_4, H_2, CO_2); .f) pH, g) total alkalinity and total CO_2.

Extended data. Figure 5: Acoustic plumes over the Horseshoe volcanic structure. a) Southward 3D view of the horseshoe morphology and two water column acoustic plumes observed on the western internal flank. b) Processed polar echogram from one EM122 multibeam ping of the data set displayed in (a) acquired on May 18th (05:41 UT) horizontal and vertical-axes correspond respectively to the cross-track distance and the water depth, in meters) – see also Acoustic plume movie 2.

Extended data. Figure 6: **Seismicity.** Top: map views, bottom: cross-sections (A-A') projection along azimuth N115°E; (B-B') along azimuth N45°E. a) Earthquakes recorded by

Paper published in Nature Geoscience , https://doi.org/10.1038/s41561-021-00809-x, Free-to-read: https://rdcu.be/cwd2Z

onshore seismological stations before the deployment of the Ocean bottom seismometers (OBS). Colored circles are events occuring in the first six weeks of the crisis, white circles are earthquakes in the intervening 8 months. b) Earthquakes recorded by the OBS+land stations between February 25 and May 6 2019 (pink dots). Yellow diamonds: location of the Very Low Frequency (VLF) events located in this study (see supplementary S2.3). c) Focal mechanisms of the largest earthquakes from the Harvard CMT catalog [40] with color scale as in a).

Extended data. Figure 7 - Global Navigation Satellite System (GNSS) data modelling and seafloor subsidence estimated from seafloor pressure variations. a) Stations locations. Arrows with colors and names: GNSS velocity vectors (mm/yr) and station names. Coloured numbers: vertical deformation (mm/yr). Inset: yellow dots : pressure sensors on ocean bottom seismometer stations (see supplementary Fig.S2.1), red arrows: Mayotte GNSS velocity vectors (mm/yr), white arrows: far field GNSS velocity vectors. b) GNSS Time series with relative displacements recorded on the east (top), north (middle) and vertical (bottom) components of the stations between January 2018 and January 2020. c) Best fit-models with 1σ uncertainties of the GNSS data for one isotropic point source and a triple volumetric discontinuity pCDM source. d) Top panel: Pressure recorded by Seabird SBE37 gauges at the six ocean-bottom seismometer stations (Yellow dots inset Figure 7a and Fig. S2.1) de-tided and converted to vertical motion. Middle panel: vertical deformation estimated at each seafloor instrument location, using the best isotropic source model obtained from the GNSS data for the March 1st to May 1st 2019 period.

Extended data. Figure 8: **Conceptual model for the Mayotte seismo-volcanic event**. Circles and diamonds are events as in Extended data - Figure 6. Focal mechanisms of main earthquakes are from Harvard CMT catalog [40]) with the same color scale as the May 10 to June 30, 2018 events, Yellow circle and blue patch: Location, with 3 sigma uncertainties, of the most robust isotropic source deformation model. a) Map view: The redish ellipse: Mayotte ridge, dashed circular area: old caldera structure in the morphology b) Cross-section (projection along azimuth 115 degree). Symbols as in a). Red lines: magma migration (dykes). Red ellipses and circle: magma reservoirs or mushes. Pink arrow: possible downsag along caldera structures. Redish zone: Eastern segment of the Mayotte ridge.

Paper published in Nature Geoscience , https://doi.org/10.1038/s41561-021-00809-x, Free-to-read: https://rdcu.be/cwd2Z

Extended data. Figure 9: Regional volcano-tectonic setting of the submarine eruption offshore Mayotte. a) Volcano-tectonic setting of the new volcanic edifice (NVE). Volcanic cones and ridges (purple) from this study and [13,72,16,51]. Beach balls: focal mechanisms for M>5 earthquakes [40]. Dotted white arrow: dyking event along the N130° E trending eastern segment of the volcanic ridge. Pink ellipse: inferred main volcano-tectonic ridges. Purple ellipses: highly damaged zones in between the en echelon ridges. Dashed grey lines: Mesozoic fracture zones [6]. Inset: sandbox model adapted from [58] illustrating the possible arrangement of the main volcano-tectonic structures in Comoros. Thick black arrows: local extensi

a

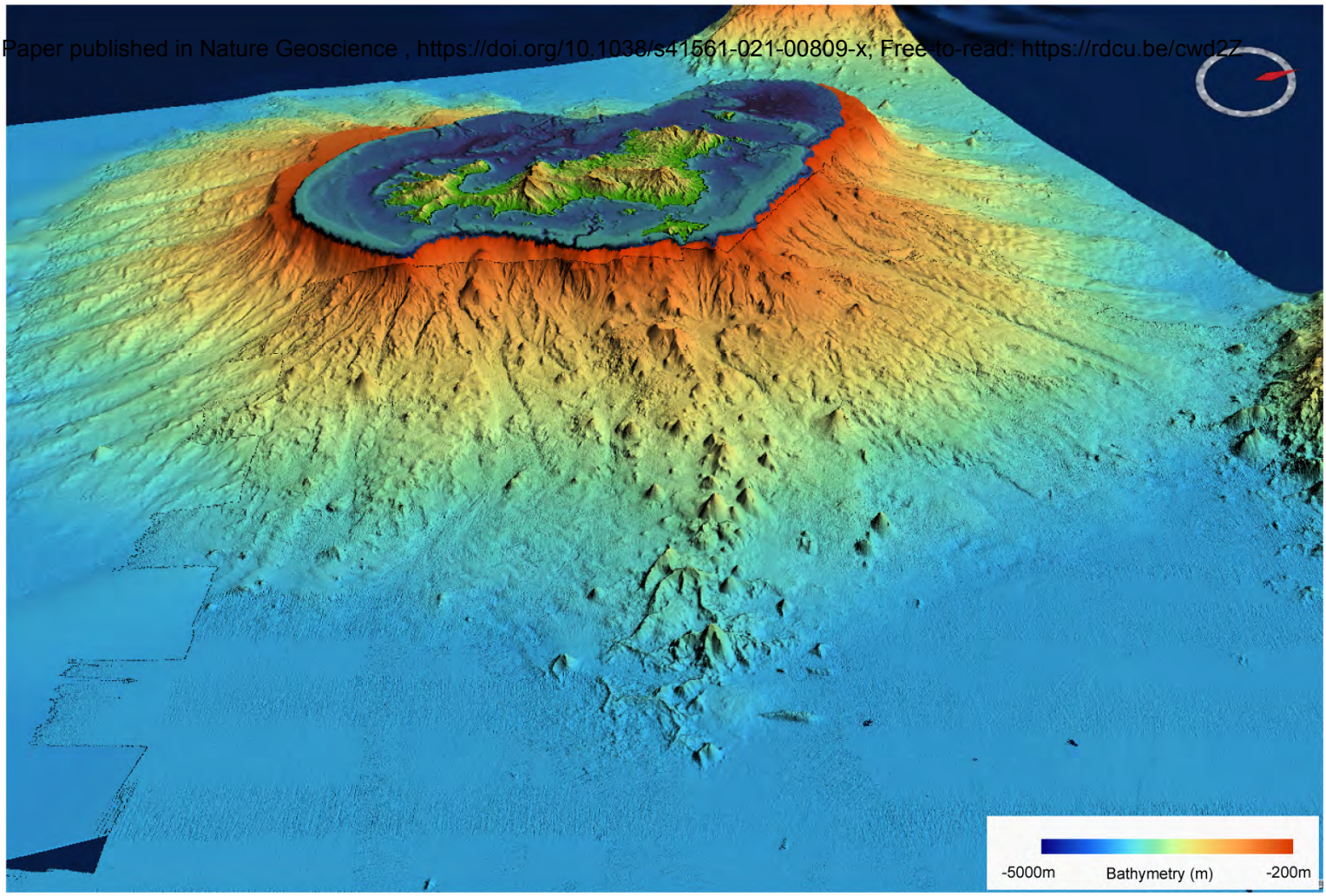

b

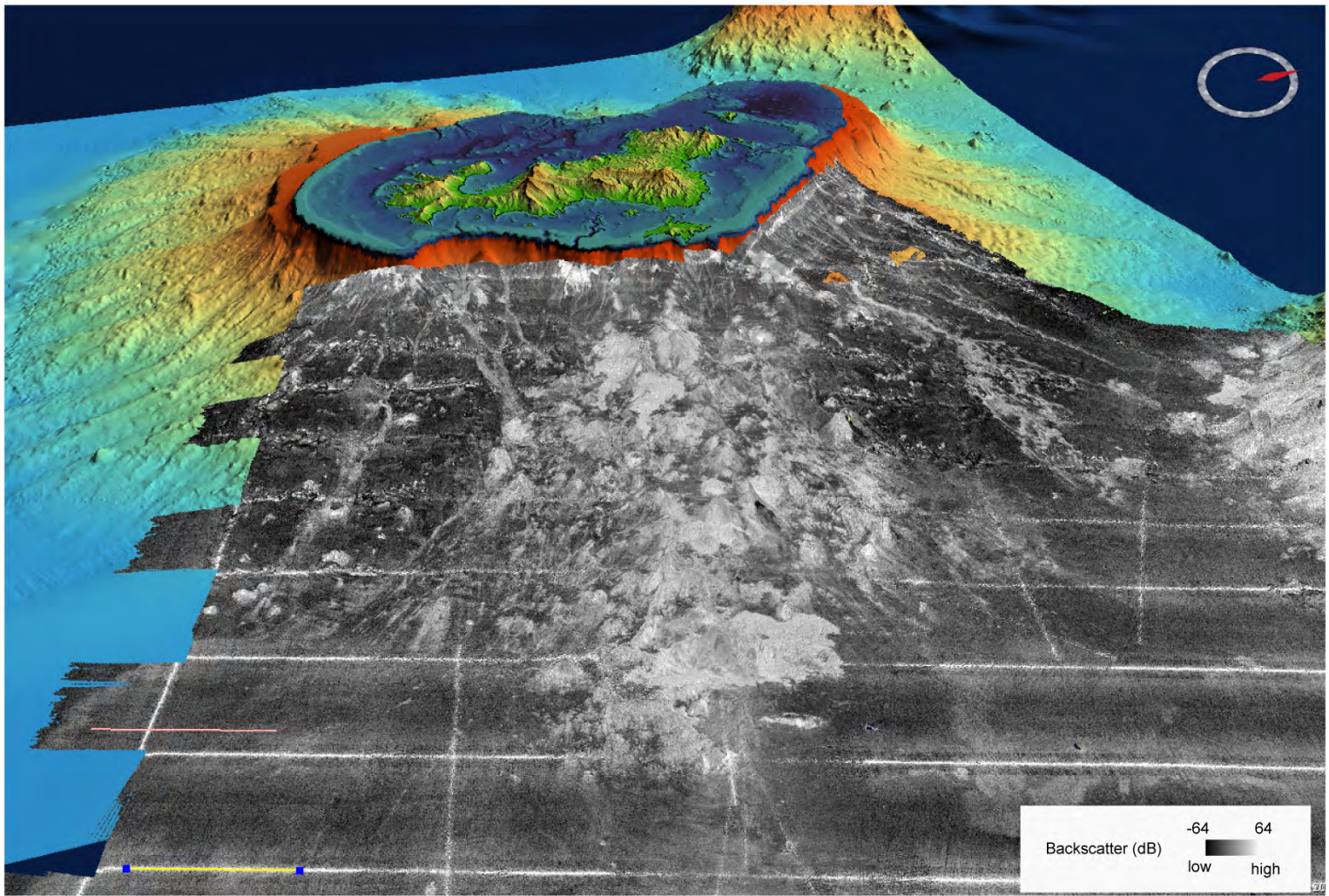

Paper published in Nature Geoscience , https://doi.org/10.1038/s41561-021-00809-x, Free-to-read: https://rdcu.be/cwd2Z

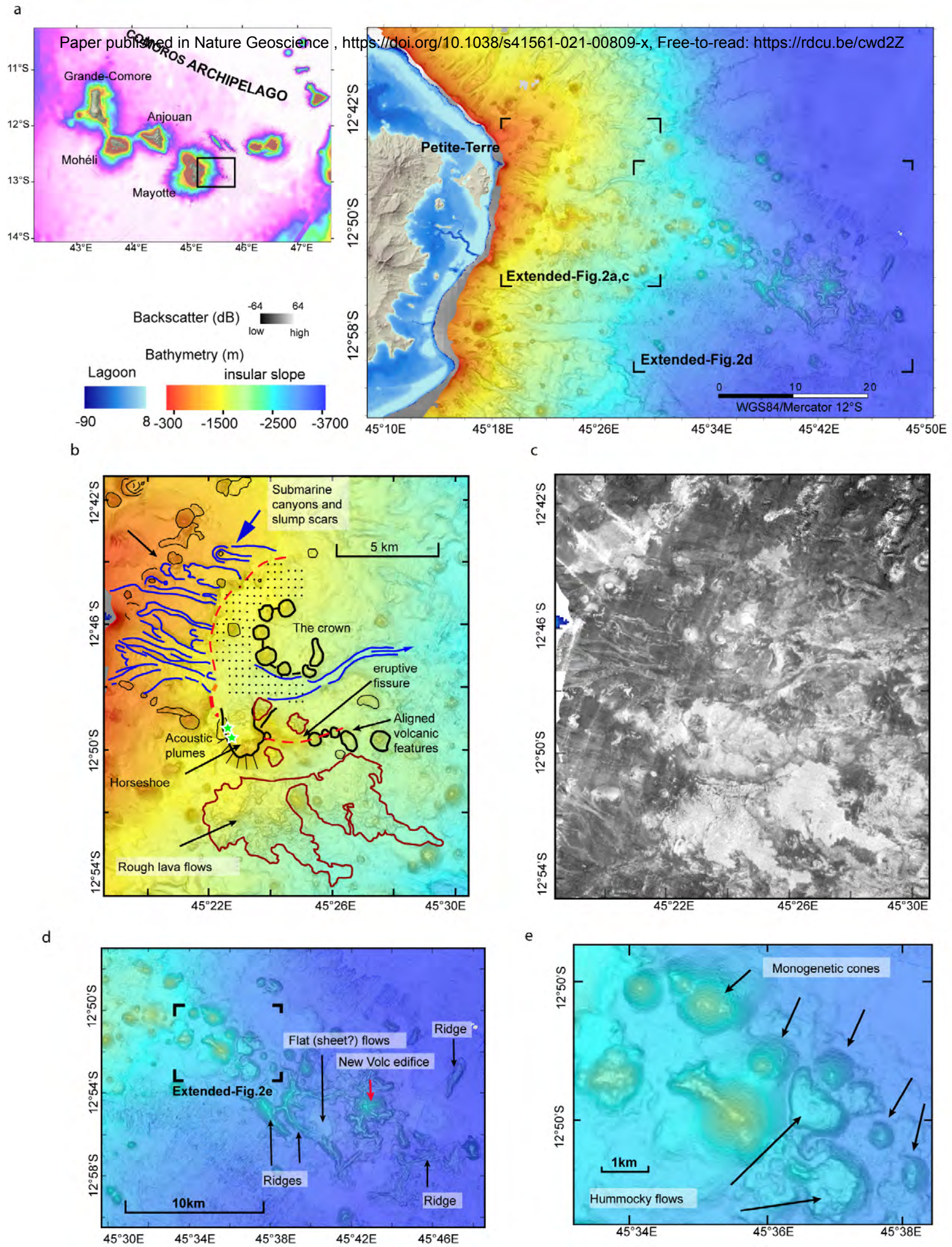

Paper published in Nature Geoscience , https://doi.org/10.1038/s41561-021-00809-x, Free-to-read: https://rdcu.be/cwd2Z

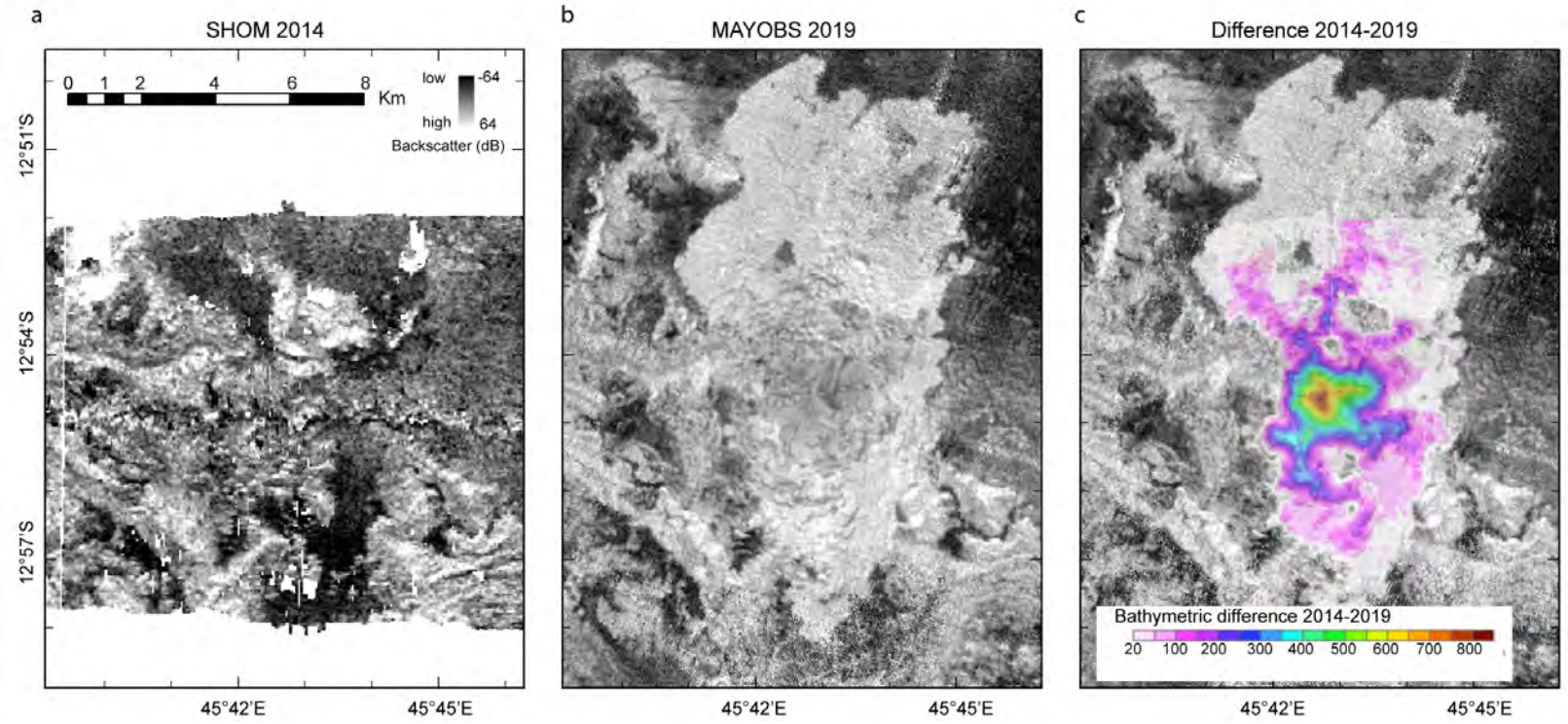

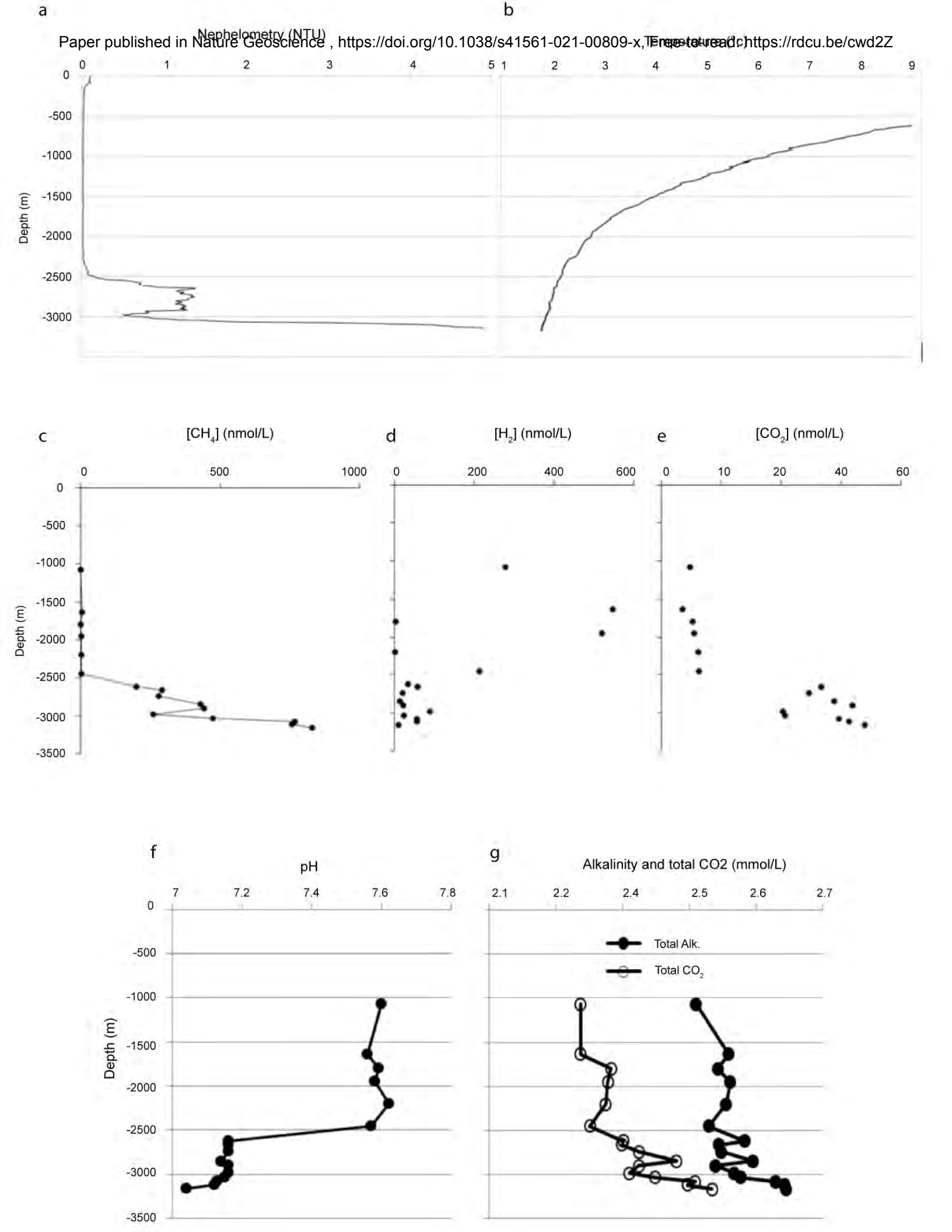

Paper published in Nature Geoscience , https://doi.org/10.1038/s41561-021-00809-x, Free-to-read: https://rdcu.be/cwd2Z

a

b

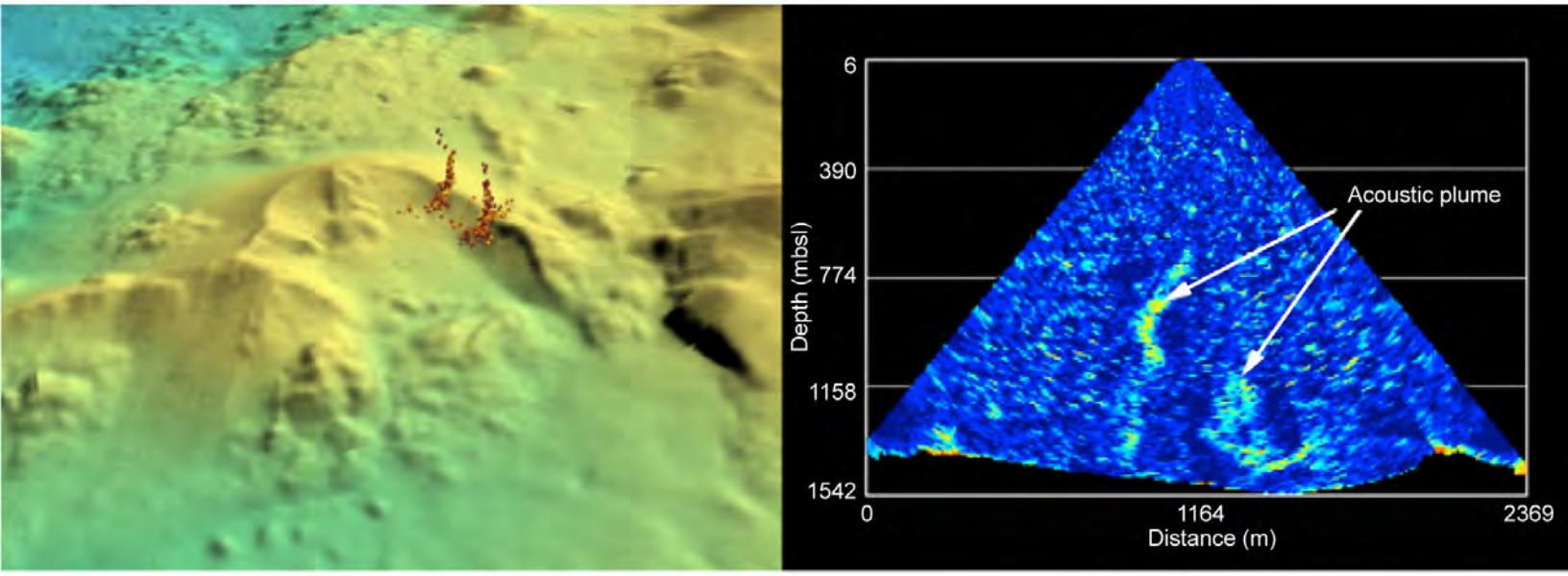

Paper published in Nature Geoscience , https://doi.org/10.1038/s41561-021-00809-x, Free-to-read: https://rdcu.be/cwd2Z

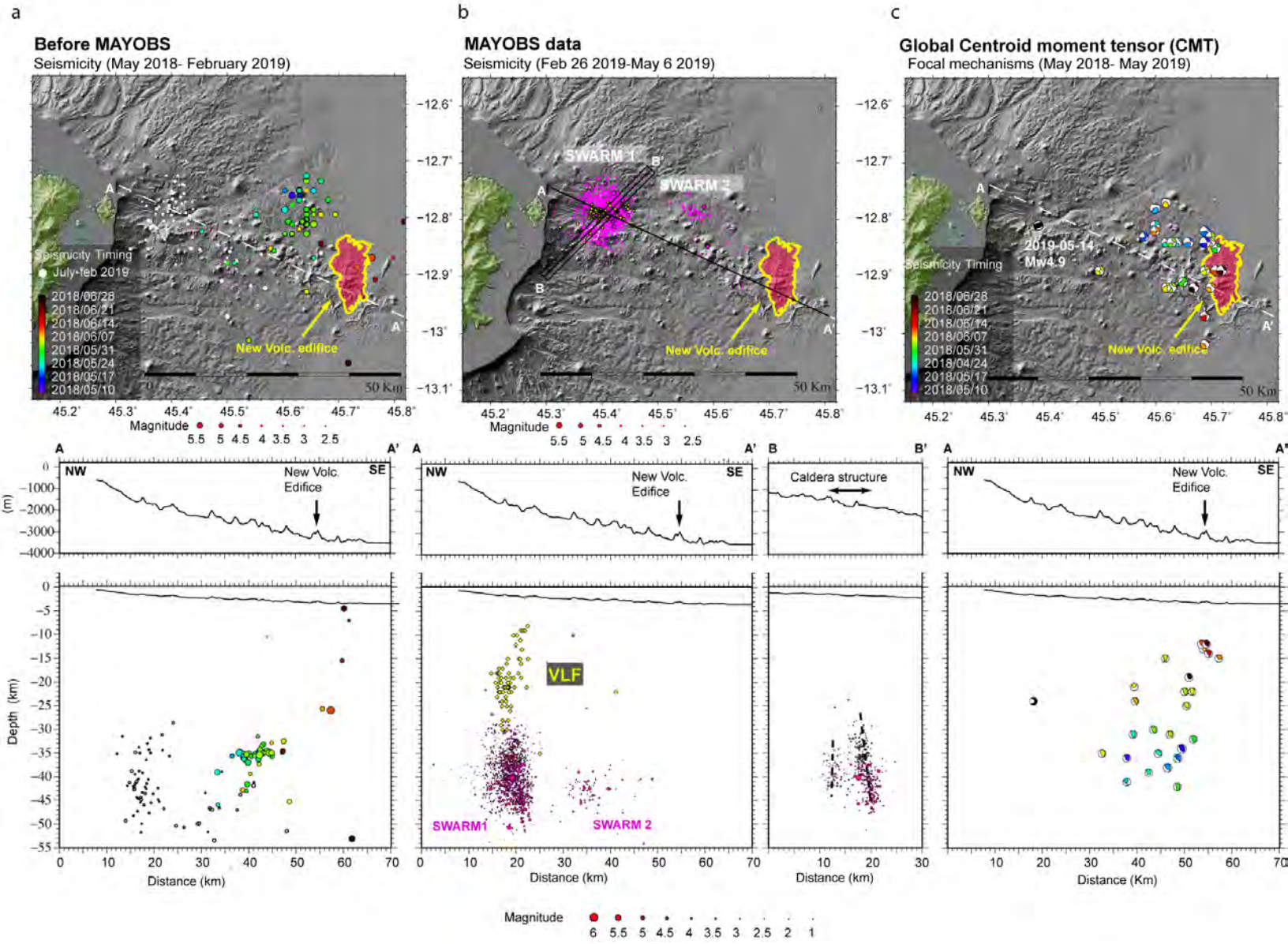

Paper published in Nature Geoscience , https://doi.org/10.1038/s41561-021-00809-x, Free-to-read: https://rdcu.be/cwd2Z

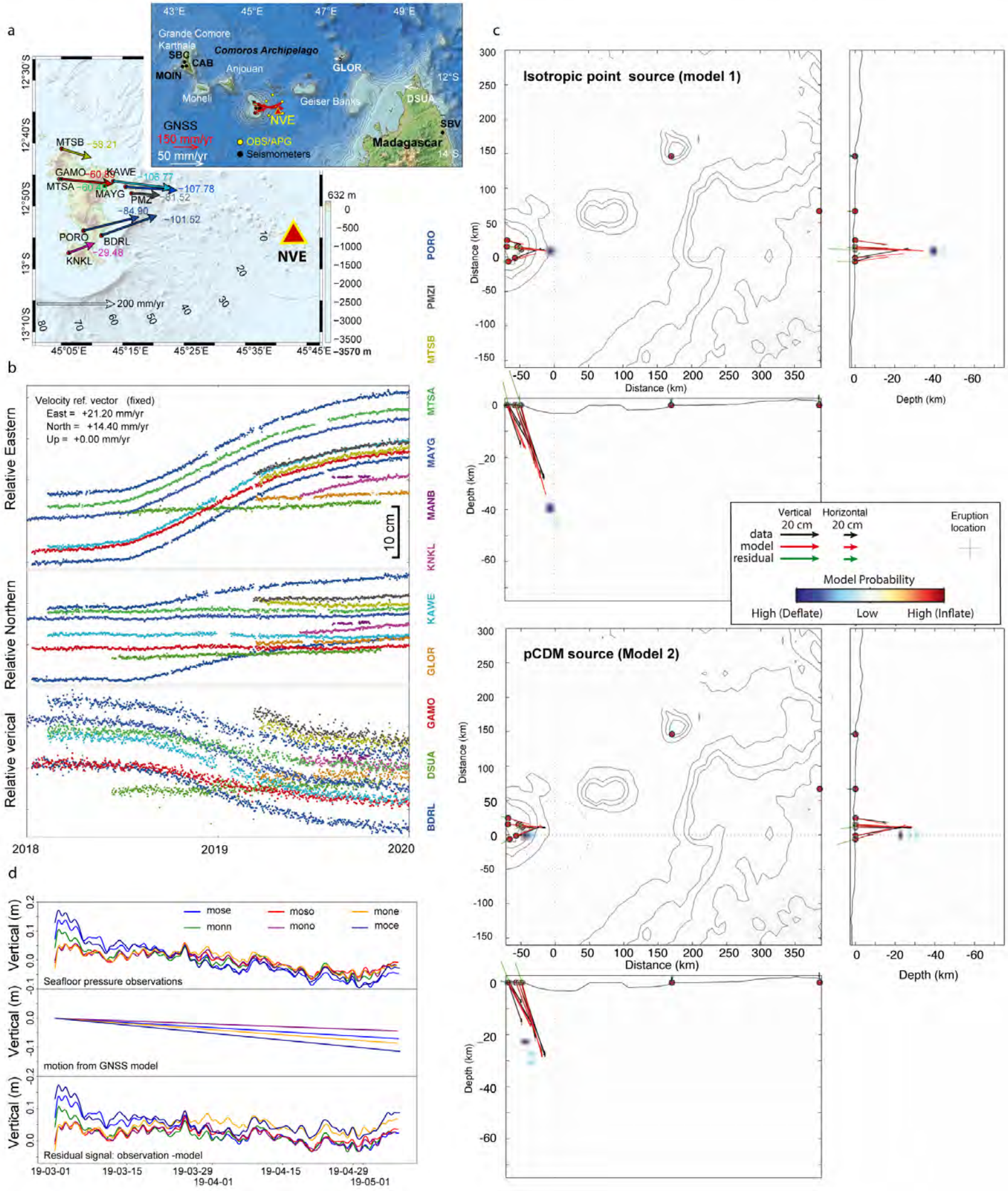

Paper published in Nature Geoscience , https://doi.org/10.1038/s41561-021-00809-x, Free-to-read: https://rdcu.be/cwd2Z

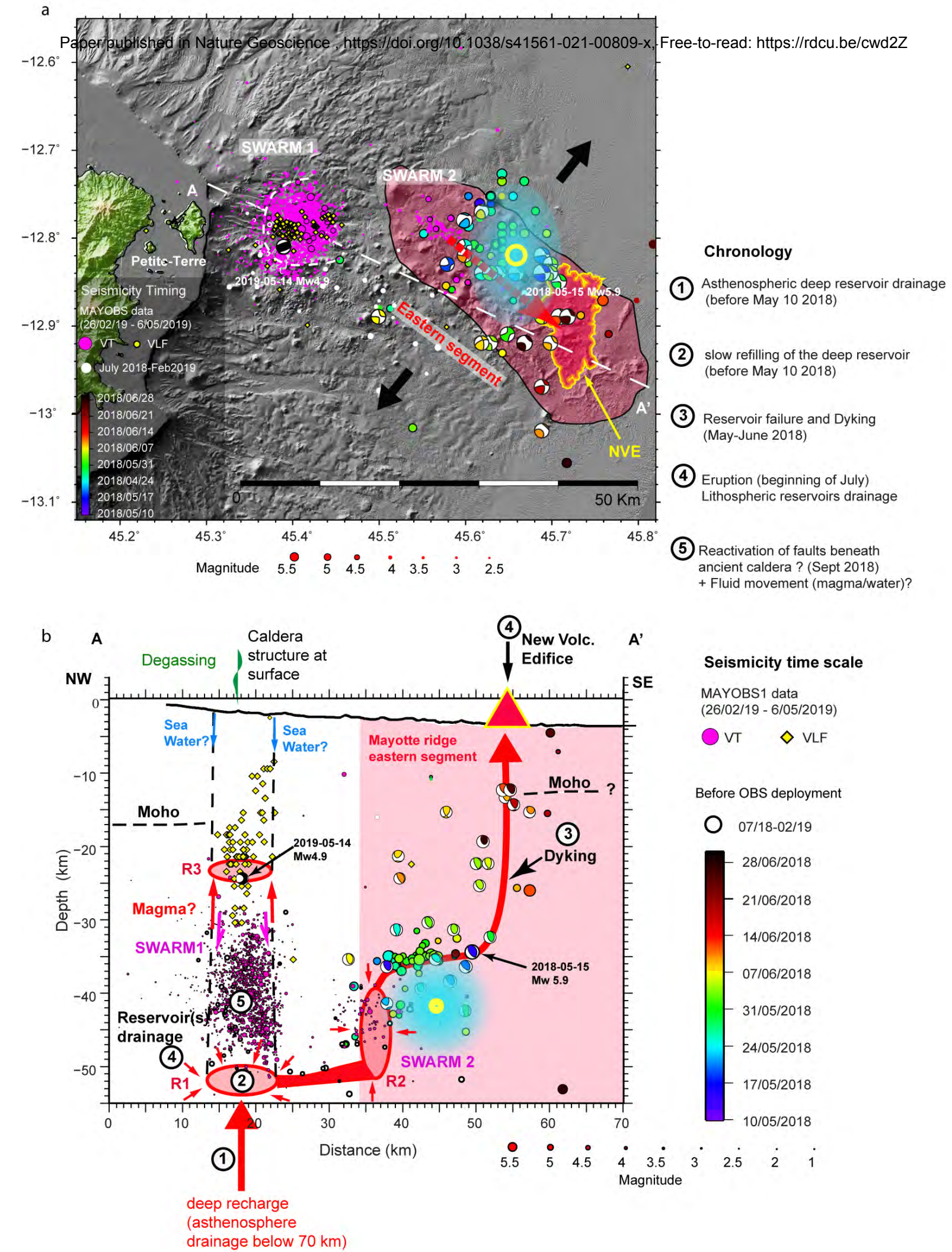

Paper published in Nature Geoscience , https://doi.org/10.1038/s41561-021-00809-x, Free-to-read: https://rdcu.be/cwd2Z

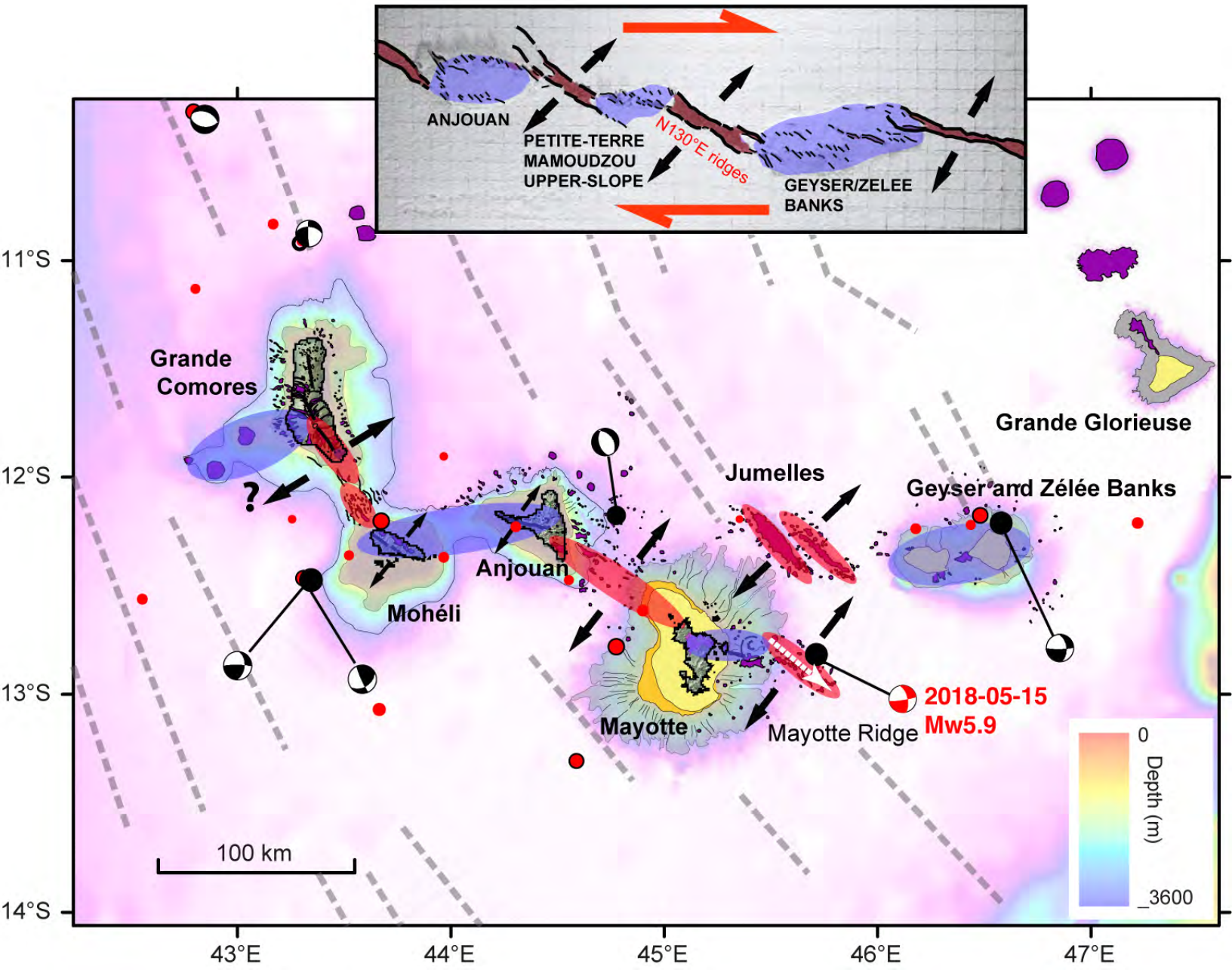

Paper published in Nature Geoscience , https://doi.org/10.1038/s41561-021-00809-x, Free-to-read: https://rdcu.be/cwd2Z

Supplement for " Birth of a large volcanic edifice offshore Mayotte via lithosphere-scale dike intrusion"

Nathalie Feuillet[1,*], Stephan. Jorry[2], Wayne C. Crawford[1], Christine Deplus[1], Isabelle Thinon[3], Eric Jacques[1], Jean Marie Saurel[1], Anne Lemoine[3], Fabien Paquet[3], Claudio Satriano[1], Chastity Aiken[2], Océane Foix[1], Philippe Kowalski[1], Angèle Laurent[1], Emmanuel Rinnert[2], Cécile Cathalot[2], Jean-Pierre Donval[2], Vivien Guyader[2], Arnaud Gaillot[2], Carla Scalabrin[2], Manuel Moreira[1], Aline Peltier[1], François Beauducel[1,4], Raphaël Grandin[1], Valérie Ballu[5], Romuald Daniel[1], Pascal Pelleau[2], Jérémy Gomez[1], Simon Besançon[1], Louis Geli[2], Pascal Bernard[1], Patrick Bachelery[6], Yves Fouquet[2], Didier Bertil[3], Arnaud Lemarchand[1], Jérome Van der Woerd[7].

1. Université de Paris, Institut de physique du globe de Paris, CNRS, F-75005 Paris, France
2. IFREMER, Unité Géosciences Marines, Technopole La Pointe du Diable, 29280 Plouzané, France
3. Bureau de Recherches Géologiques et Minières - BRGM, DGR/GBS, F-45060 Orléans, France
4. Université Grenoble Alpes, IRD, ISterre
5. LIttoral ENvironnement et Sociétés (LIENSs) UMR7266, Université de La Rochelle - CNRS, 2 rue Olympe de Gouges, 17000 La Rochelle
6. Université Clermont Auvergne, CNRS, IRD, OPGC, Laboratoire Magmas et Volcans, F-63000 Clermont-Ferrand, France,
7. Institut de Physique du Globe de Strasbourg UMR7516 CNRS Université de Strasbourg, 5 rue René Descartes 67000 Strasbourg, France

Paper published in Nature Geoscience , https://doi.org/10.1038/s41561-021-00809-x, Free-to-read: https://rdcu.be/cwd2Z

Description of contents

This document contains three main sections S1, S2, S3 with supplementary text, figures and tables.

S1 includes two tables (S1.1 and S1.2) and presents the analysis of the rock sample DR01.

S2 includes text, 18 figures (Fig. S2-1 to S2-18) and 2 tables (Tables S2.1, S2.2) and presents the seismological data and analysis. Classical high frequency earthquakes are presented in section S2.2 and very low frequency events in section S2.3.

S3 includes three tables (Tables S3.1 to S3.3) and text and presents the Global Navigation Satellite System GNSS and seafloor pressure data and modeling (see also Extended data Fig. 7).

Paper published in Nature Geoscience , https://doi.org/10.1038/s41561-021-00809-x, Free-to-read: https://rdcu.be/cwd2Z

S1. Analysis of rock sample DR01

See Figure 2a in the main text for the position of dredge DR01.

Composition of representative rocks of the New Volcanic Edifice (DR01).

Sample name	**DR 01 – 01**	**DR 01 – 05**
SiO_2	45.98	45.72
TiO_2	3.21	3.20
Al_2O_3	14.88	14.81
Fe_2O_3 t	13.77	13.76
MgO	5.28	5.27
MnO	0.23	0.23
CaO	7.07	7.04
Na_2O	4.55	4.48
K_2O	2.43	2.44
P_2O_5	1.64	1.62
LOI	0.17	0.34
Total	**99.21**	**98.91**

Table S1.1: Analysis* recalculated to 100 wt% on an anhydrous basis, with Fe2O3 = 0.2 total Fe.

Sample name	**DR 01 – 01**	**DR 01 – 05**
SiO_2	46.95	46.91
TiO_2	3.28	3.28
Al_2O_3	15.19	15.19
Fe_2O_3	*2.81*	*2.82*
FeO	*10.12*	*10.16*
MgO	5.39	5.41
MnO	0.23	0.24
CaO	7.22	7.22
Na_2O	4.65	4.60
K_2O	2.48	2.50
P_2O_5	1.67	1.66
Total	100.00	100.00
$Na_2O + K_2O$	7.13	7.10

Table S1.2: Analysis* recalculated to 100 wt% on an anhydrous basis

***** *Major elements were analysed by ICP-AES (Horiba Jobin-Yvon Ultima C spectrometre) at Laboratoire Magmas et Volcans (Clermont-Ferrand, France), after alkali fusion and nitric acid dissolution, following the method described by* (Gurioli, Di Muro et al. 2018)*. Calibration was done against a BHVO-1 rock standard* (Jochum, Weis et al. 2016).

Paper published in Nature Geoscience , https://doi.org/10.1038/s41561-021-00809-x, Free-to-read: https://rdcu.be/cwd2Z

S2. Seismology

S2.1 General Figures

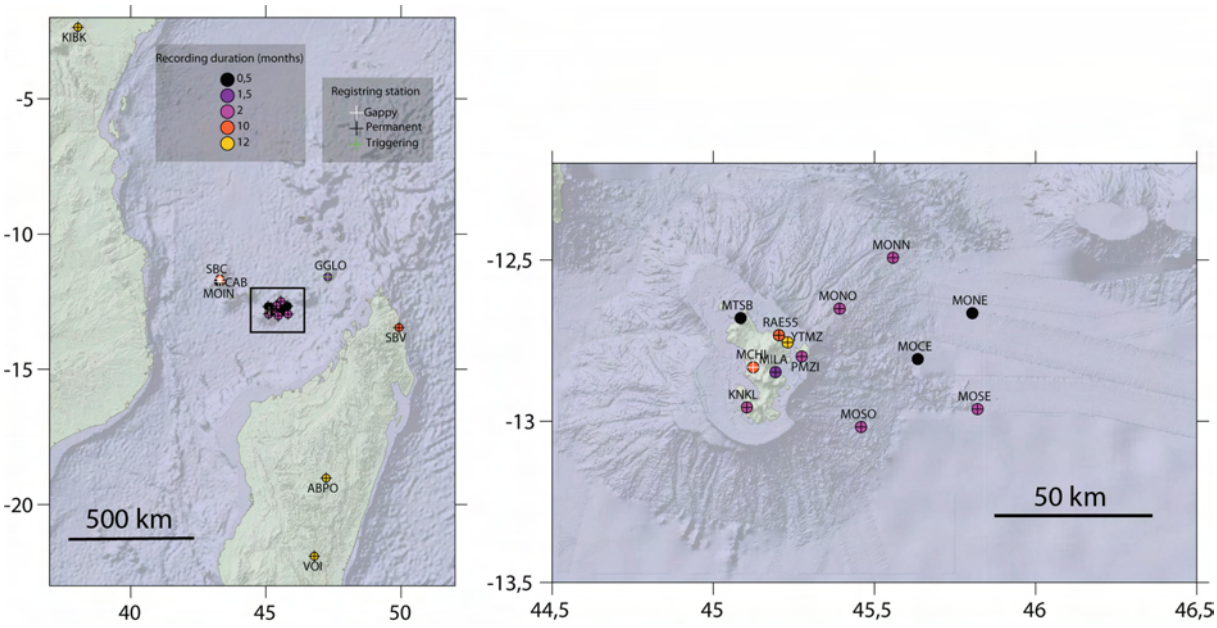

Figure S2.1: Map of seismological land stations and Ocean Bottom Seismometers (OBS) used in this study (left: regional scale; right: local scale). Colour code: months of data recorded between May 2018 and May 2019. White crosses: Stations with significant data gaps and poor data quality. GGLO station had only triggered data. A seafloor pressure gauge is attached to each OBS.

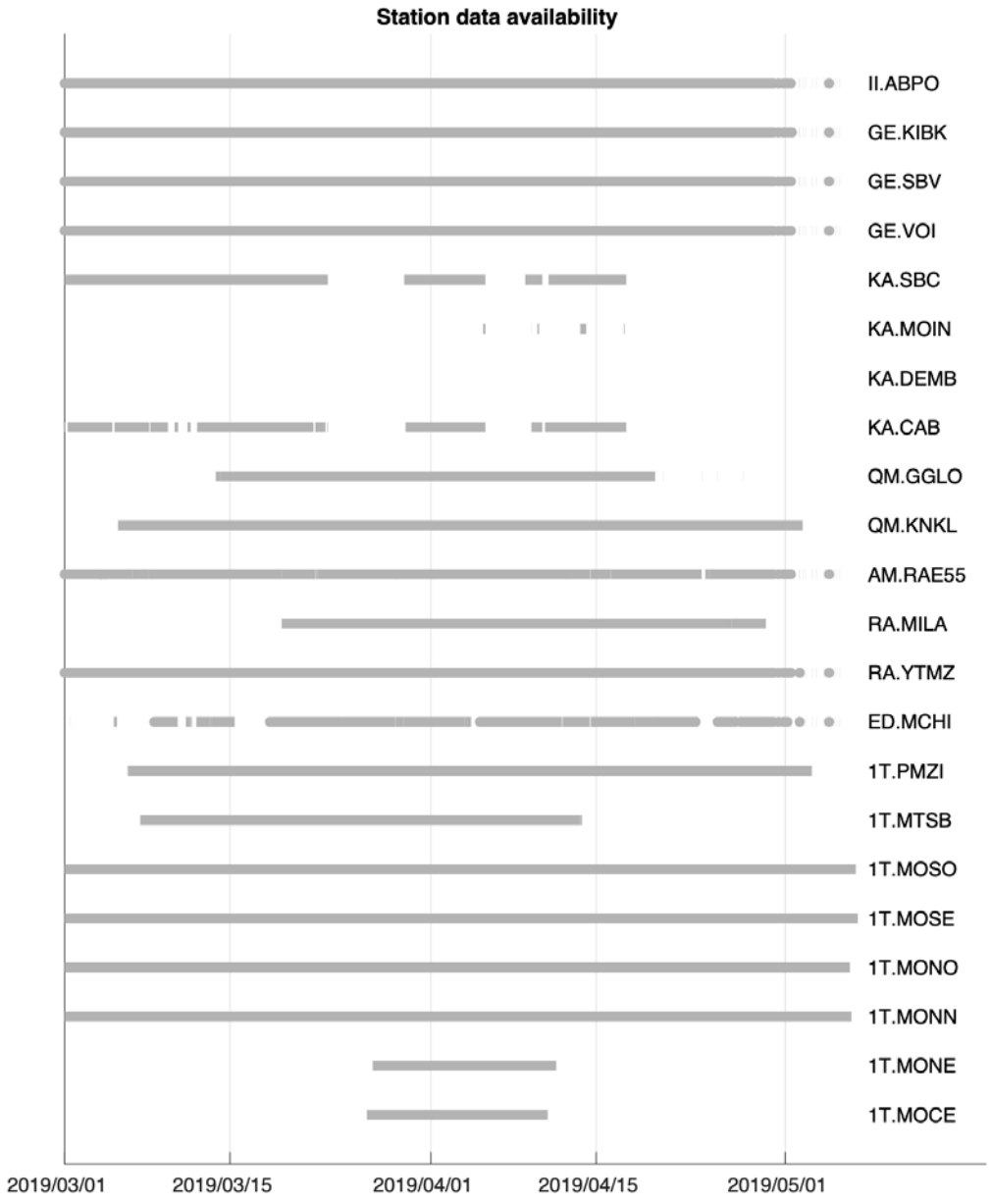

Figure S2.2: Station data availability between 25 February 2019 and 5 May 2019.

Code	Network	Name	Location	Latitude (°N)	Longitude (°E)	Elevation (m)	Duration (months)	Type
KNKL	QM	Kani-Keli	Mayotte	-12.9571	45.1042	24	2.0	VBB
RAE55	AM	Koungou	Mayotte	-12.7335	45.2036	47	10.5	SP
MCHI	ED	Chiconi	Mayotte	-12.8329	45.1237	130	10.5	BB
KIBK	GE	Kibwezi	Kenya	-2.3591	38.0433	790	12.0	VBB
SBV	GE	Sambava	Madagascar	-13.4584	49.9212	65	10.0	VBB
VOI	GE	Vohitsoka	Madagascar	-21.9065	46.7933	993	12.0	VBB
ABPO	II	Ambohipanompo	Madagascar	-19.0183	47.2292	1552	12.0	VBB
CAB	KA	Cabanes	Grande Comore	-11.7486	43.3435	1984	11.0	BB
MOIN	KA	Moindzaza	Grande Comore	-11.7659	43.2435	145	0.5	BB
DEMB	KA	Dembeni	Grande Comore	-11.8774	43.4062	300	0.6	BB
SBC	KA	Bahani	Grande Comore	-11.6491	43.2969	640	11.0	BB
GGLO	QM	Glorieuse	Glorieuse	-11.5830	47.2924	7	1.7	BB
MILA	RA	Iloni Dembeni	Mayotte	-12.8481	45.1928	30	1.6	ACC
YTMZ	RA	Mamoudzou	Mayotte	-12.7557	45.2307	25	12.0	ACC
MOCE	1T	central OBS	offshore	-12.6652	45.8037	-3120	0.5	SP
MONE	1T	NE OBS	offshore	-12.8074	45.6343	-3510	0.5	SP
MONN	1T	N OBS	offshore	-12.4932	45.5576	-3180	2.0	SP
MONO	1T	NW OBS	offshore	-12.6513	45.3919	-1600	2.0	SP
MONO	1T	NW OBS	offshore	-12.6513	45.3919	-1600	2.0	SP
MOSE	1T	SE OBS	offshore	-12.9625	45.8199	-3520	2.0	SP
MOSO	1T	SW OBS	offshore	-13.0790	45.4585	-2530	2.0	SP
MTSB	1T	Mtsamboro	Mayotte	-12.6804	45.0847	50	1.0	BB
PMZI	1T	Pamandzi	Mayotte	-12.7993	45.2743	10	2.0	BB

Table S2.1: Stations used for local earthquake relocations

VBB: Very BroadBand (high performance, low frequency cutoff > 120s)

BB: BroadBand (medium to standard performance, low frequency cutoff > 20s)

SP: Short Period (low frequency cutoff < 1s)

ACC: Accelerometer

Paper published in Nature Geoscience , https://doi.org/10.1038/s41561-021-00809-x, Free-to-read: https://rdcu.be/cwd2Z

S2.2: Earthquake locations and magnitudes

S2.2.1: Velocity models

Once phases were picked on the OBS data (see Methods, location of stations in Fig. S2.1 and information on data Station data availability Fig. S2.2), Hypo71(Lee and Lahr 1972) was used for preliminary earthquake location and SeisComP3 (Weber, Becker et al. 2007) was used to compute M_L and M_{Lv} magnitudes. We started with two different velocity profiles. The first one, named "Coffin449", is based on a Vp velocity profile calculated from a 1986 active-seismic sonobuoy experiment (Coffin, Rabinowitz et al. 1986). The second profile, named "ADofal" is based on a Vs velocity profile from a receiver function study (Dofal, Fontaine et al. 2018) using a Mayotte land station. After picking the first 100 events, we used a modified Wadati diagram (Chatelain 1978) to estimate a local (OBS and Mayotte land stations) Vp/Vs ratio of 1.6 and a regional (Glorieuse, Karthala, Madagascar, Kenya, Seychelles and Réunion Island stations) Vp/Vs of 1.72 (Figure S2.3).

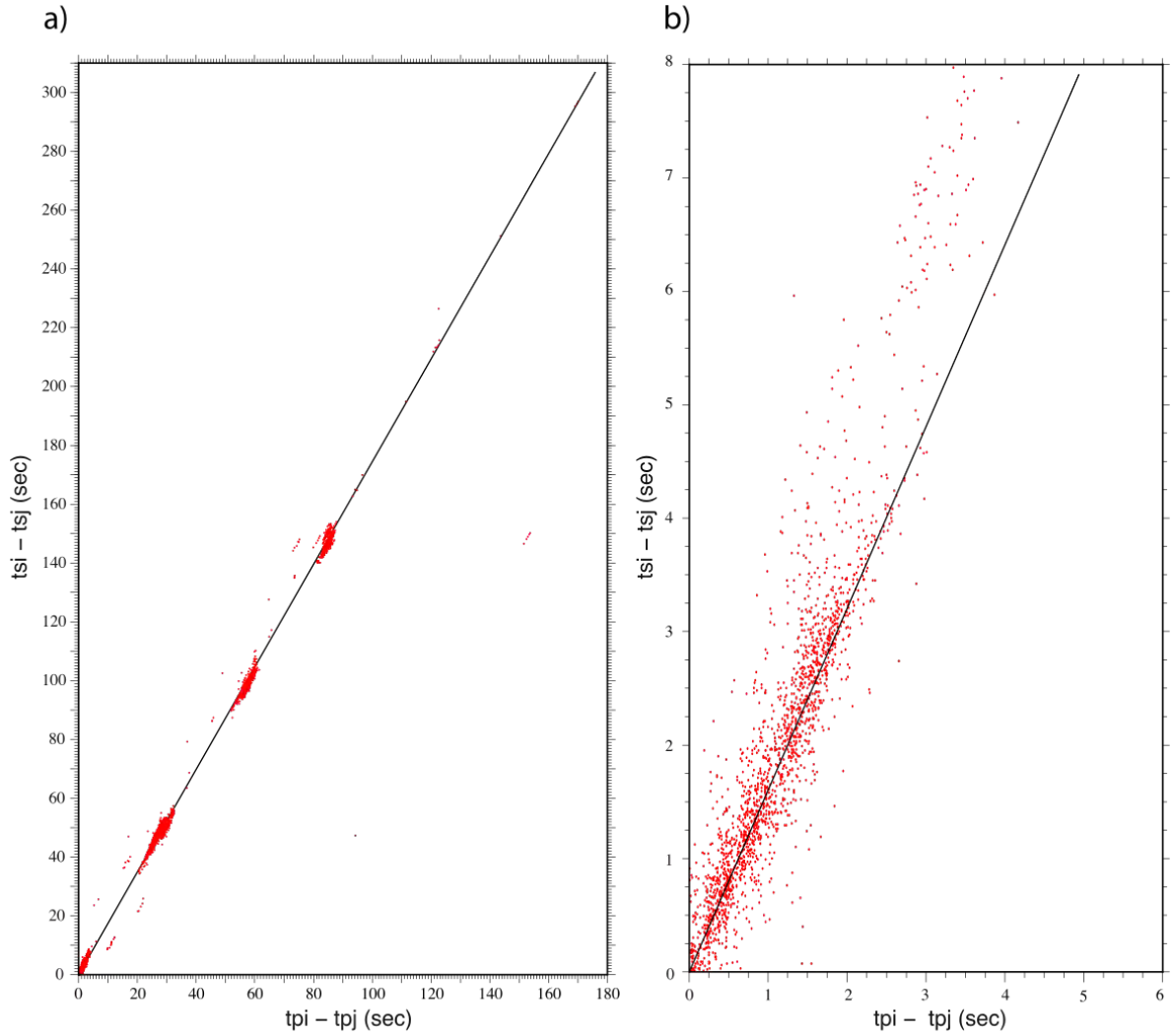

Figure S2.3: Modified Wadati diagram (Chatelain 1978) of arrival times of the P-and S-waves for the first hundred OBS+land located earthquakes. Differences in arrival times of S-wave arrival times (tsi, tsj) are plotted against differences in P=wave arrival times (tpi, tpj) for station couples(i,j) (a) Plot for local and regional stations: Vp/Vs = 1.72. (b) Plot for local stations only (Mayotte land stations and and OBSs): Vp/Vs = 1.6.

We then used NonLinLoc (Lomax, Michelini et al. 2009) to relocate the events. We first focused on local picks, in order to assess the best local velocity. We compared the distributions of maximum hypocentre error for the two velocity models and three Vp/Vs ratios (Figures S2.4 and S2.5) for an 800-earthquake dataset. The ellipsoidal error major axes range between 2 and 10 km, with most of the events having error major axes of 4±2 km. The best results were obtained using the "ADofal" velocity model with Vp/Vs = 1.66, for which 83.5% of the events had errors smaller than 5km. Our final velocity model is a hybrid model

composed of: the "ADofal" and Vp/Vs 1.66 for OBSs and stations in Mayotte; the "Coffin449" oceanic model and Vp/Vs 1.72 for regional stations (between 200 and 400 km from Mayotte); AK135 (Kennett, Engdahl et al. 1995) for more distant stations. NLL also computes a Vp/Vs ratio for each event, based on P and S arrival times, and independent from earthquake location, using a formulation described in the HypoEllipse manual (Lahr 1999). The NLL estimation, using the 800 events, supports the mean Vp/Vs ratios of 1.66 use for local stations and 1.72 for regional stations (Figure S2.6).

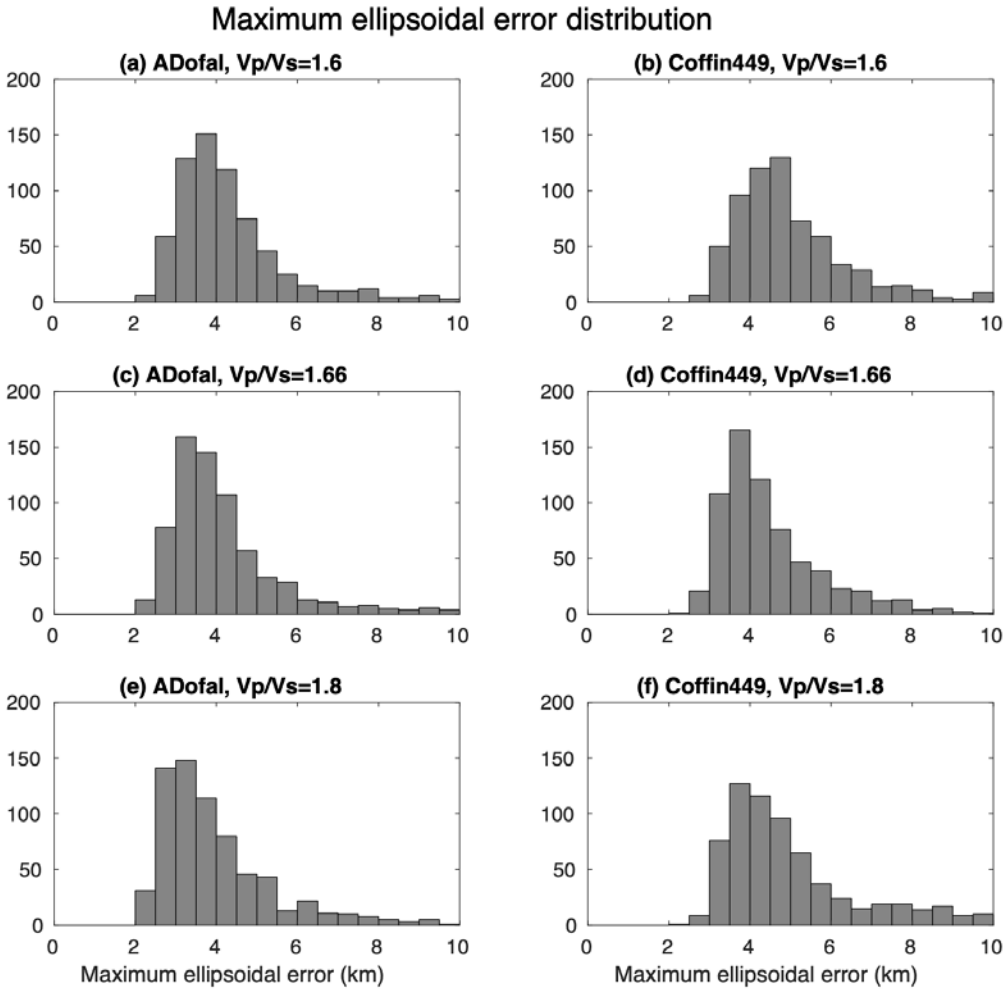

Figure S2.4: Histogram of the maximum ellipsoidal errors (major axis) for the 800 earthquakes picked using the OBS+land network, for six tested velocity models. For each Vp/Vs ratio, the ADofal model shows a lower distribution than the Coffin449 model. The dispersion is lowest for Vp/Vs = 1.66.

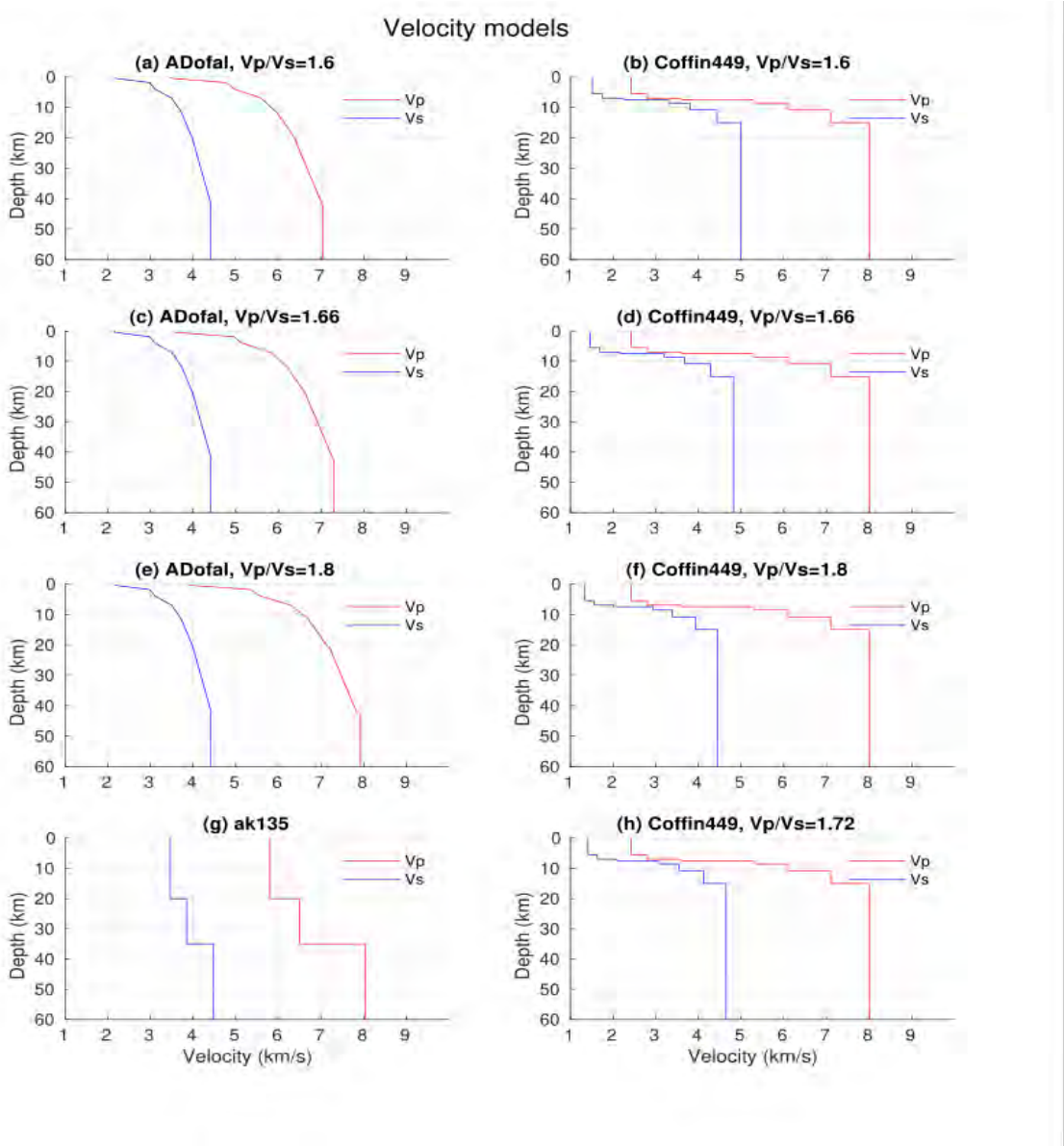

Figure S2.5: The 1D, layered velocity models tested to locate the 800 earthquakes picked on the local OBS+land network.

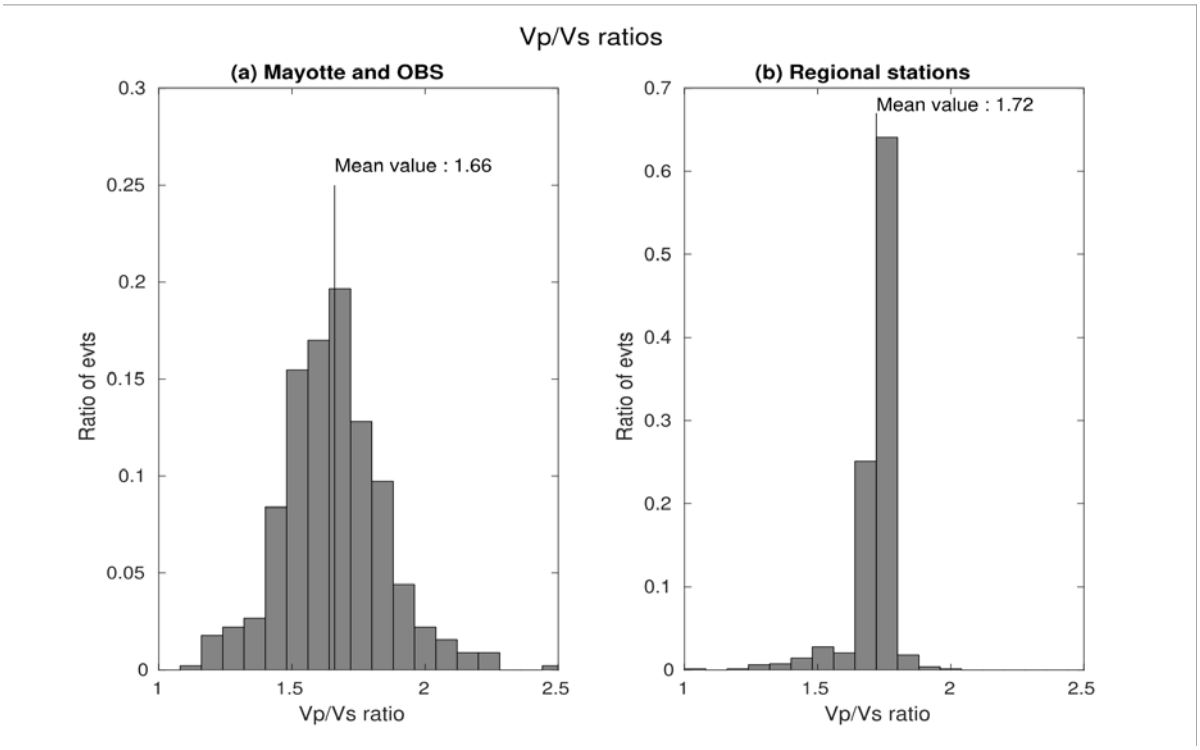

Figure S2.6: Distribution of P-wave velocity/S-wave velocity (Vp/Vs) ratios based on NonLinLoc estimations, from local (a) and regional (b) phases for the 800 events. The mean values agree with the initial values found using a limited subset of events and the modified Wadati method (Chatelain 1978) (Figure S2.3).

S2.2.2 Depth bounds of events

The resulting locations span a depth range between 25 and 55 km, with average vertical uncertainty of 2.5 km (Figure S2.7). These depths are stable over most of the velocity models and Vp/Vs ratios (Figure S2.8): only the "Coffin449" oceanic crust type model, with an unrealistic Vp/Vs ratio of 1.8, gives significantly shallower depths, between 10 and 40 km. In no case were earthquakes located shallower than 10 km.

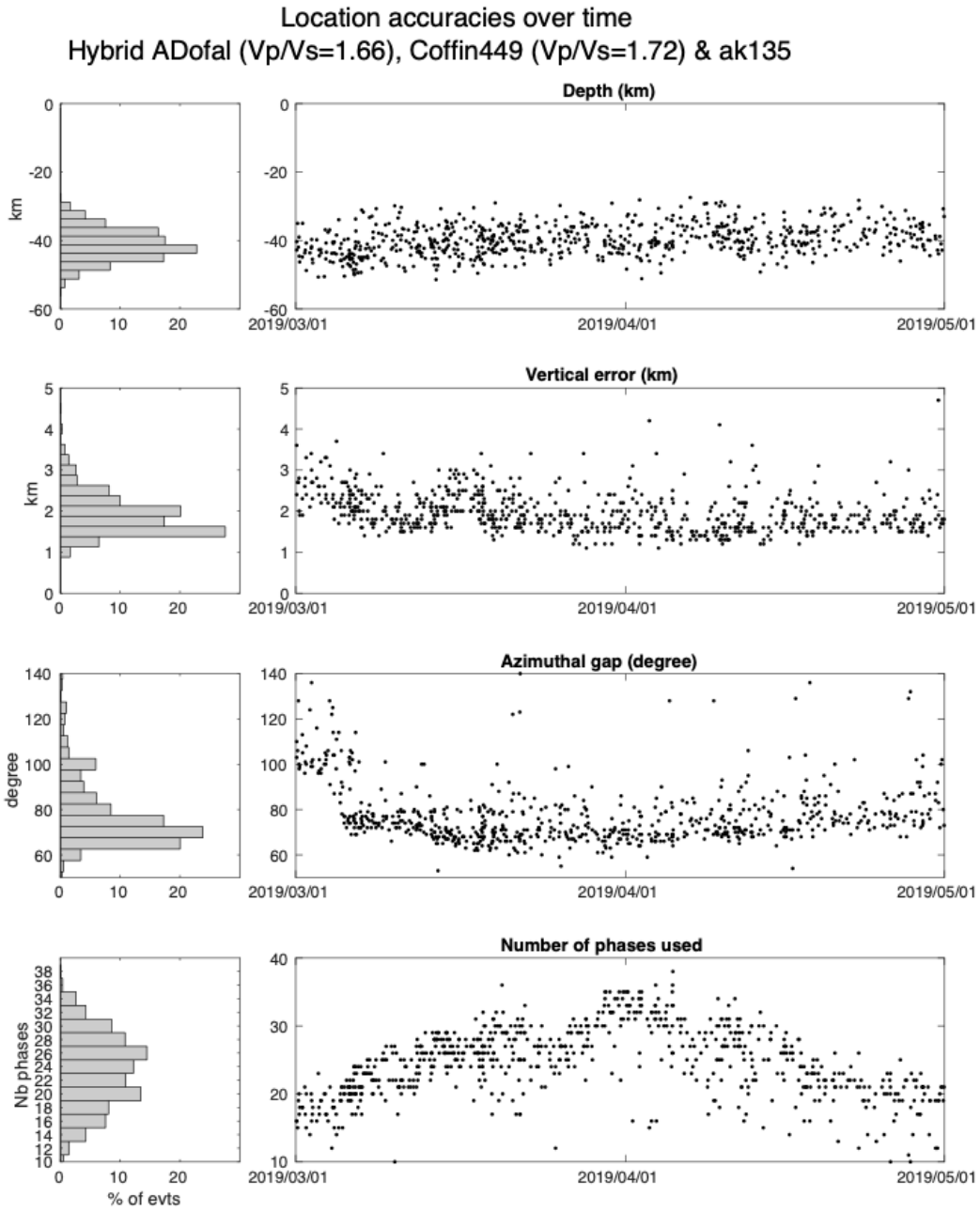

Figure S2.7: Distributions (left panel) and time evolutions (right panel) for the 800 earthquakes recorded by the Ocean Bottom Seismometers between February 26 and May 5, 2019 and located onboard. Upper panel: hypocentral depths; second panel: depth uncertainties; third panel: azimuthal gaps; bottom panel: the number of P- and S-wave phases used.

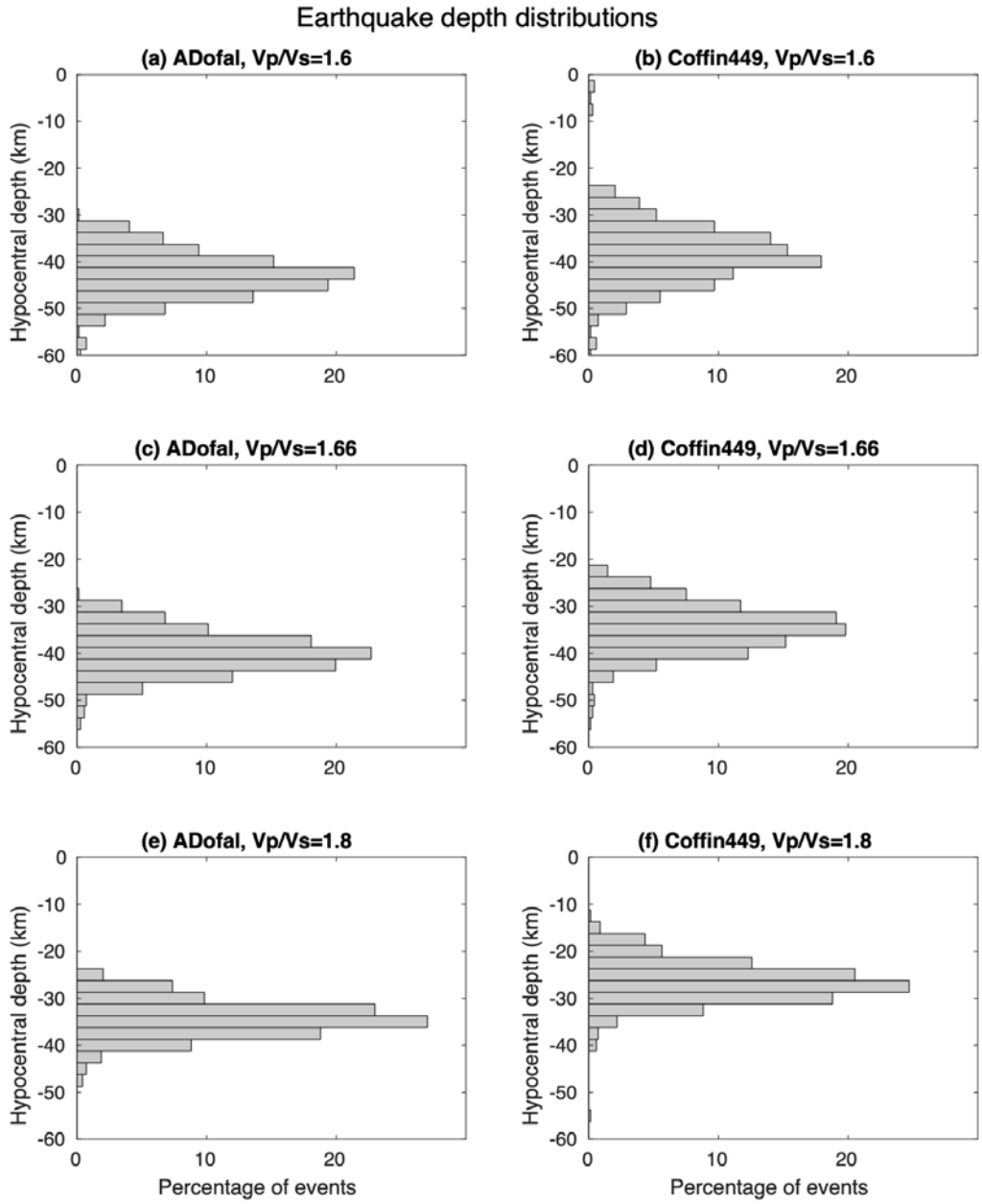

Figure S2.8: Distribution of the hypocentral depths of the OBS+land catalogue, for each tested velocity model.

We performed three tests to verify the unusual depth of the hypocenters. For these tests, we selected a high quality sub-set of the catalog, consisting of events, with at least 5 P-wave and 5 S-wave arrivals picks on the OBS data (149 events). In the first test, we relocated the earthquakes using half-space velocity models with Vp between 2 and 9 km/s and a Vp/Vs ratio of 1.65. In the second test, we added a 200m-thick very low velocity (0.2 km/s,

consistent with soft unconsolidated sediments (Grevemeyer, Hayman et al. 2019) Figure S2.9 to the ADofal model. In the third test we calculated hypocenters using only P-arrivals

All of the half-space tests returned depths greater then 15km and, for a reasonable half-space P-wave velocity (5-7 km/s), the depths range between 20 and 60 km (except for a few locations with convergence problems, Table S2.2). The second test returned depths concentrated between 22 and 47 km (compared to 25 and 50 km using our hybrid model (Figure S2.9), indicating that a superficial unconsolidated sediment layer would only have a small effect on the depth distribution. The mean RMS with this model is higher than that for our original model. Finally, using only P arrivals does not significantly change the depths.

Half space Velocity model	Mean RMS (s)	Depth range (km)	Percentage and Depth range (km) of events with convergence problem
2km/s	4.89	15-25	
3km/s	2.45	15-30	
4km/s	1.28	15-35	
5km/s	0.65	20-40	4% : 10-15km
6km/s	0.33	25-50	4% : 5-15km
7km/s	0.32	25-55	3% : 5-35km
8km/s	0.49	30-60	3% : 5-30km
9km/s	0.65	35- >60	4% : 5-35km

Table S2.2: Effect of different half-space velocity models (VP/VS = 1.65) on the earthquake depth distribution. Hypocenters calculated using Hypo71. The last column shows the percentage and depth range of events with convergence problems (RMS generally greater than 1s).

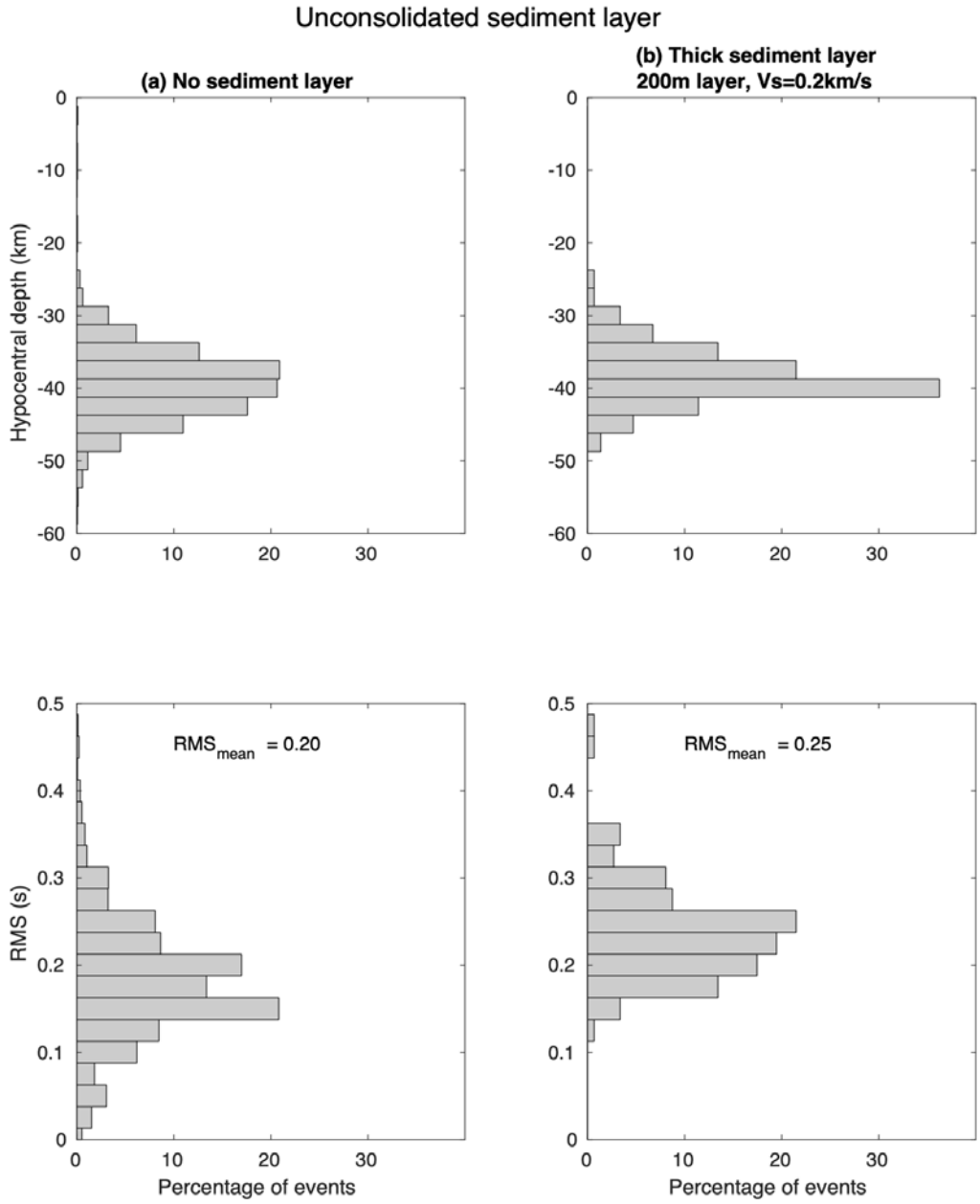

Figure S2.9: Effect on Depth and Rms distributions of adding an unconsolidated sediment layer below the OBSs. Hypocentres calculated using NLL. Depth and Rms distributions for relocations using a) our chosen hybrid model. b) the same model topped by a 200m-thick sediment layer with low S-wave velocity (0.2 km/s) below the OBSs.

S2.2.3 Relocation of a subset of events before the OBS deployment

We used NLL and the above-described hybrid velocity model to relocate a small subset of the events that occurred before the OBS deployment, including data from the Karthala stations

(network KA, Table S2.1) that had not previously been taken into account (data not available in 2018). We relocated 139 of the strongest events, 56 of which were between May and June 2018 (the beginning of the seismic crises). The location accuracy, which depends strongly on the network geometry, changes over time (Figure S2.10).

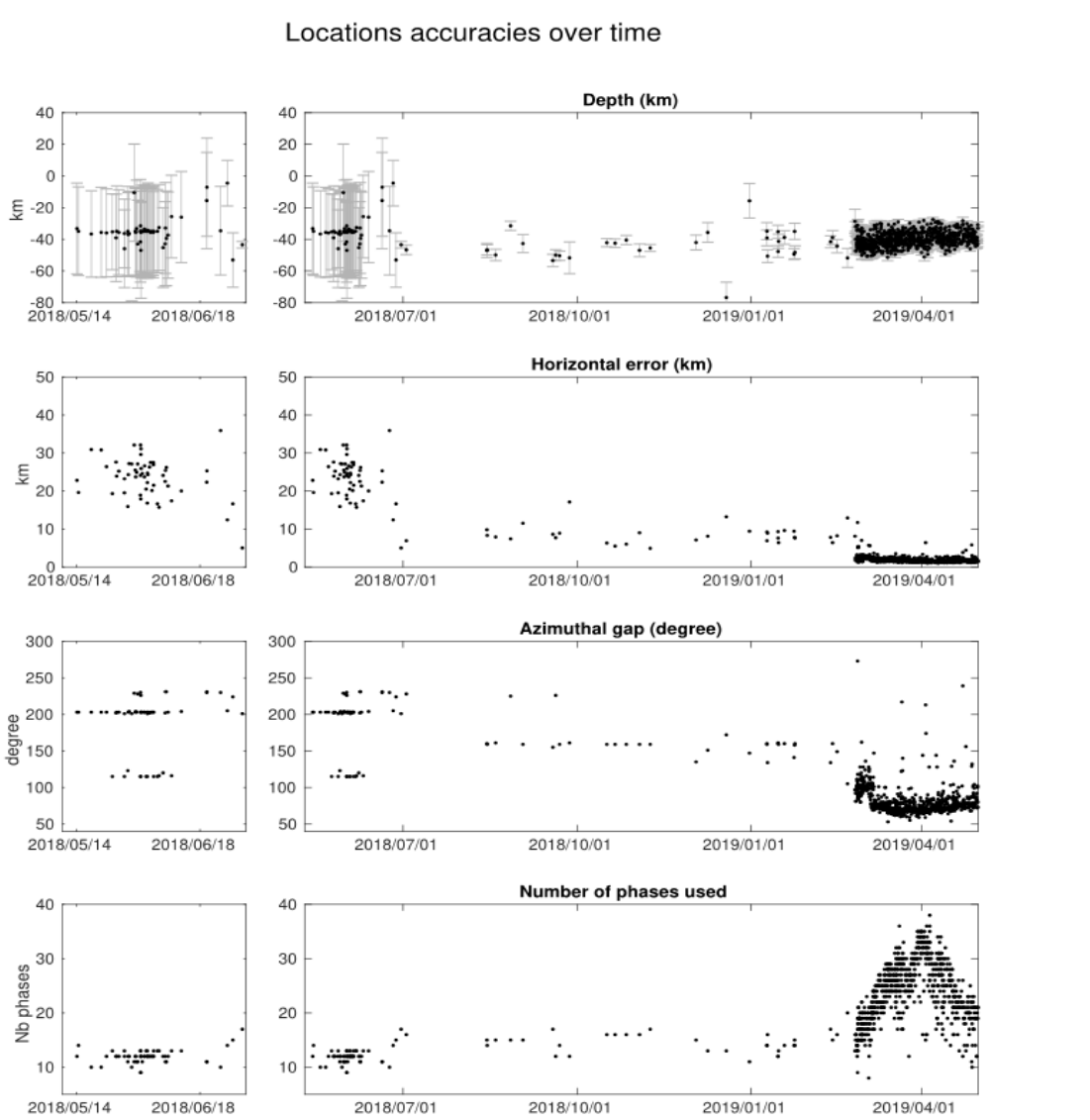

Figure S2.10: Evolution of location statistics from May 2018 to May 2019 for the 800-event OBS+land catalogue plus the 139-event relocated pre-OBS catalogue. Left panels: Zoomed-in view on the first month. Upper panel: hypocentral depths and errors bars; second panel: epicentral location errors; third panel: azimuthal gap of station coverage; lower panel: number of P-and S phases used.

S2.2.4 Magnitude estimation

We used the embedded ML (all channels) and MLv (vertical channel) magnitude formulae in SeisComP3 to compute the earthquake local magnitudes. SeisComP3 converts the signal to a Wood-Anderson seismometer response. There is no systematic difference between ML and MLv magnitudes.

Because no moment tensors were computed by global agencies during the deployment period, we couldn't calibrate the attenuation values used in the magnitude computation. However, 38 of the events were also located by the United States Geological Survey (USGS), and we compared our magnitudes to theirs (Figure S2.11). All USGS values are mb body wave magnitudes at teleseismic distances, except one which is a W-phase tensor magnitude. The scatter is large for this limited sub-set of events, but the global fit between USGS magnitudes and our local magnitudes has a regression close to one.

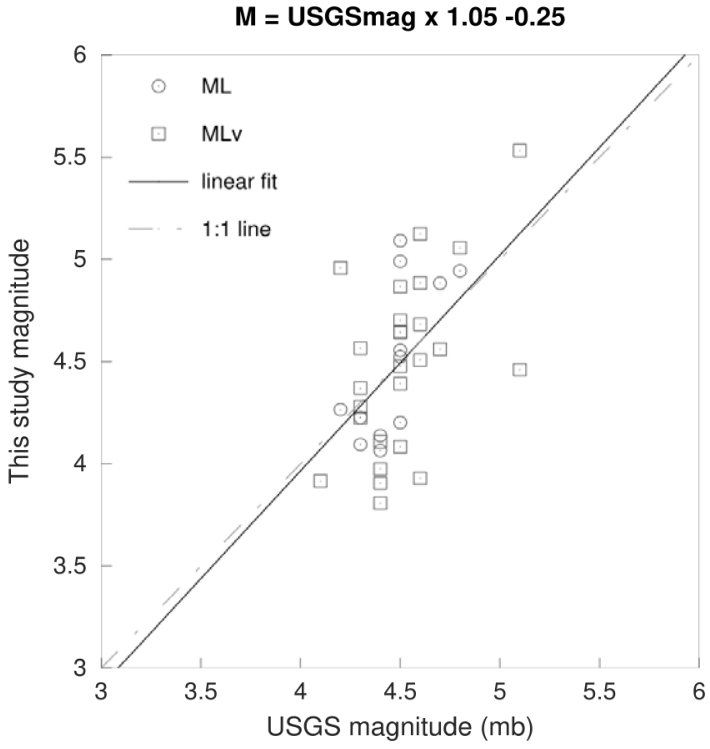

Figure S2.11: Comparison of this study's local magnitudes and USGS magnitudes. The relations between the magnitudes are scattered on either side of the 1:1 line.

S2.3. Very low frequency (VLF) event detection and location

We detected 84 VLF events between February 25 and April 24, 2019, using the recordings of the OBSs' wideband hydrophones. Events were detected using an STA/LTA trigger (Withers, Aster et al. 1998) on traces filtered in the 10-20 s period band. We use an STA window of 100 s, an LTA window of 600 s and a trigger threshold of STA/LTA ≥ 3. An event was declared when at least one station triggered. A post-processing step was performed to remove events without a clear ~15 s peak in their amplitude Fourier spectrum (e.g., large earthquakes with sufficient energy below 10 s of period), by computing the ratio between the peak amplitude of the Fourier spectrum and the average amplitude in the period band 13-18 s and only keeping events with ratio larger than 3. The resulting 135 events were visually inspected to remove remaining false detections, leaving us with 84 VLFs (Figure S2.12)

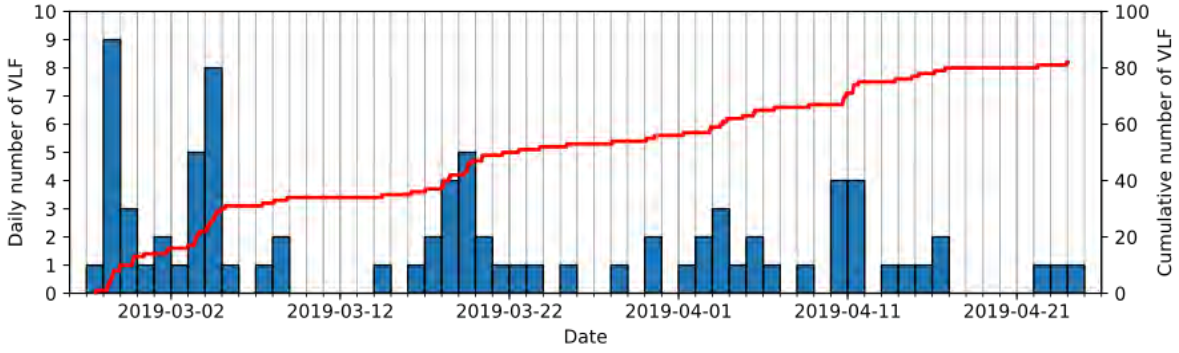

Figure S2.12: Daily and cumulative number of detected VLFs as a function of time, between February 25 and April 24, 2019.

We compared one of the highest amplitude events (February 26, 2019) with the large November 11, 2018 VLF signal recorded worldwide. Even though the November 11 event has twice the amplitude of the February 26 event on local land stations, their overall waveform shapes are similar, with three main wave packets and a duration of ~2000 s (Figures S2.13 and S2.14). The vertical and horizontal particle motions of the two events at land stations YTMZ and MCHI show a similar elliptical polarization (typical of Rayleigh

waves) with similar vertical incidence and horizontal azimuth (Figures S2.15 and S2.16). These observations indicate that the large November 11, 2018 VLF shares a similar location and source mechanism to the OBS-observed VLF activity.

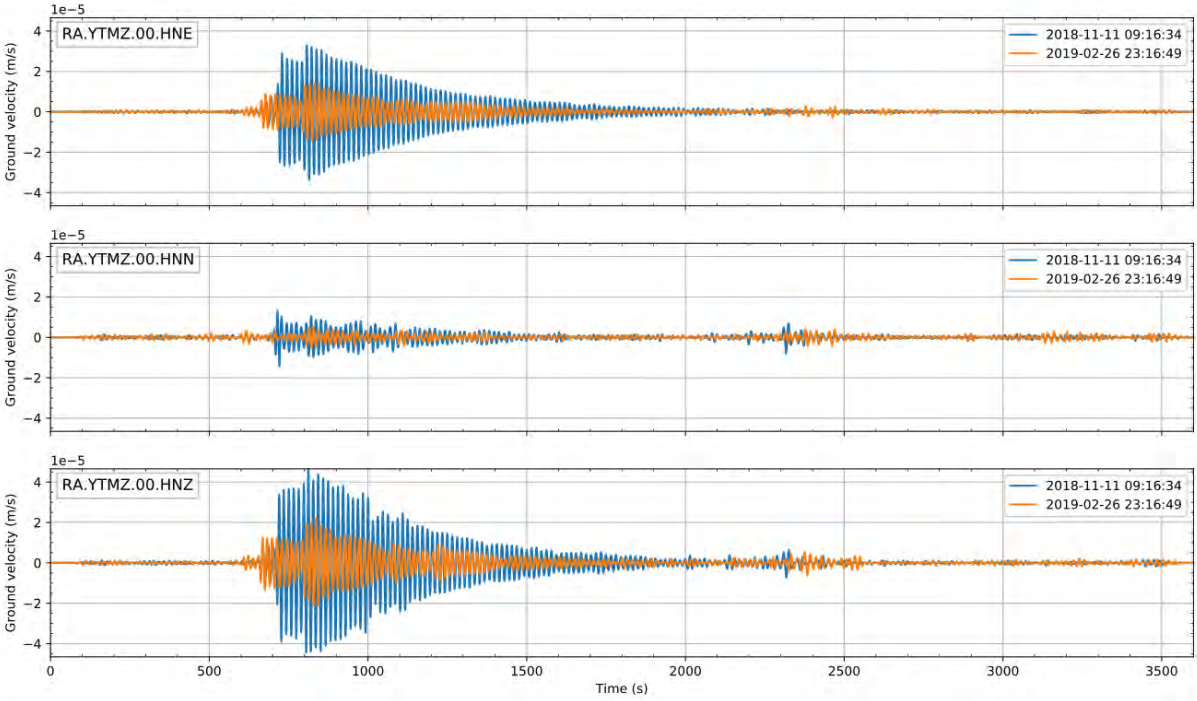

Figure S2.13: Comparison between the large November 11, 2018 VLF signal (blue), and one of the largest VLFs (February 26, 2019, orange) detected in this study. The three panels show –from top to bottom– E, N and Z components at accelerometric station YTMZ (on land), corrected by instrument response and integrated to ground velocity.

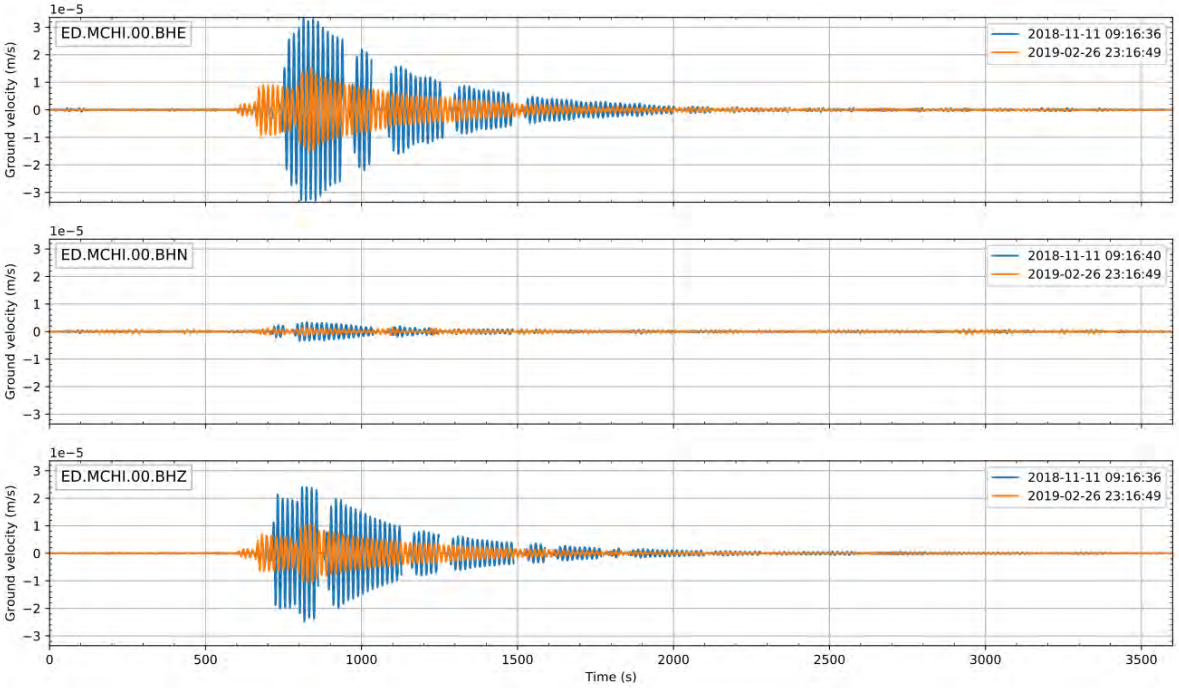

Figure S2.14: Same as Figure S2.13, but for velocimetric station MCHI (on land), corrected by instrument response. Signal for the November LF event presents data gaps due to transmission problems.

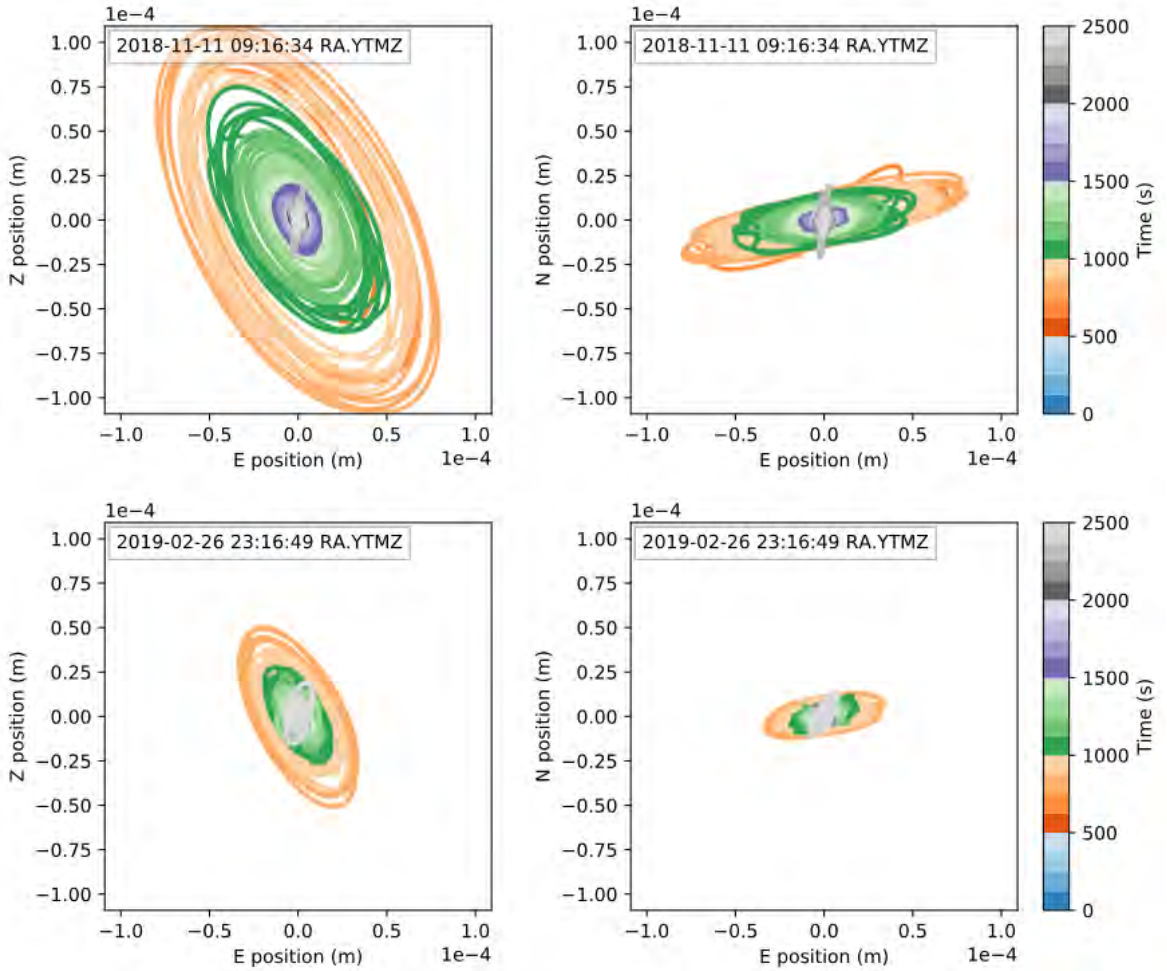

Figure S2.15: Particle motions of the large November 11, 2018 VLF signal (top panels) and one of the largest VLFs (February 26, 2019) detected in this study (bottom panels), at station YTMZ. Left panels show particle motion in the E-Z plane (vertical plane); right panels show particle motion in the E-N plane (horizontal plane). The curves are colour-coded according to time from the beginning of the trace (see Figure S2.14).

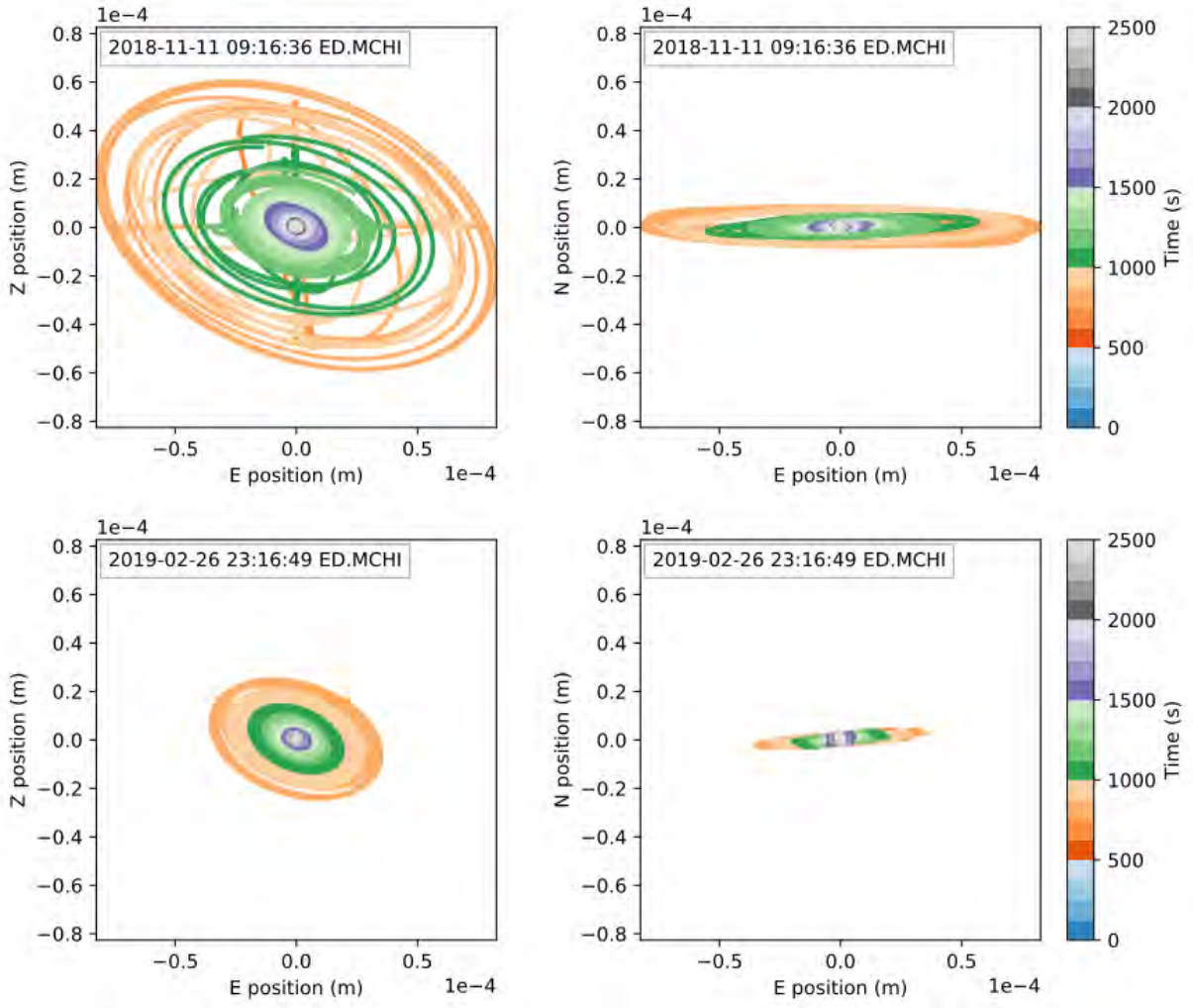

Figure S2.16: Same as Figure S2.15, but for station MCHI.

Paper published in Nature Geoscience , https://doi.org/10.1038/s41561-021-00809-x, Free-to-read: https://rdcu.be/cwd2Z

The VLF sources were located using data from the 6 OBS hydrophones plus the land stations RA.YTMZ, ED.MCHI, AM.RAE55, 1T.MTSB and 1T.PMZI (see figures S2.1 and S2.2 for station locations and availability). We first estimated the relative time delay for each station pair using vertical components of land stations, transformed to acceleration, and pressure recordings from the OBH, which correspond to accelerations at these frequencies (An, Cai et al. 2017). The local cross-correlation (LCC) between the two signals (Figure S2.17) was computed on a 20 s sliding Gaussian window (Hale 2006) for 1-bit normalized signals (Larose, Derode et al. 2004). The one-bit LCC shows that the two signals remain coherent for more than 1500 s. The monochromatic nature of the signal implies that cross-correlation values are periodic, with a period of ~15 s. We then averaged the LCC function in the time window where the signal envelope is greater than 20% of the maximum value (vertical bars in figure S2.17) to obtain a station-pair cross correlation (CC) curve as a function of lag.

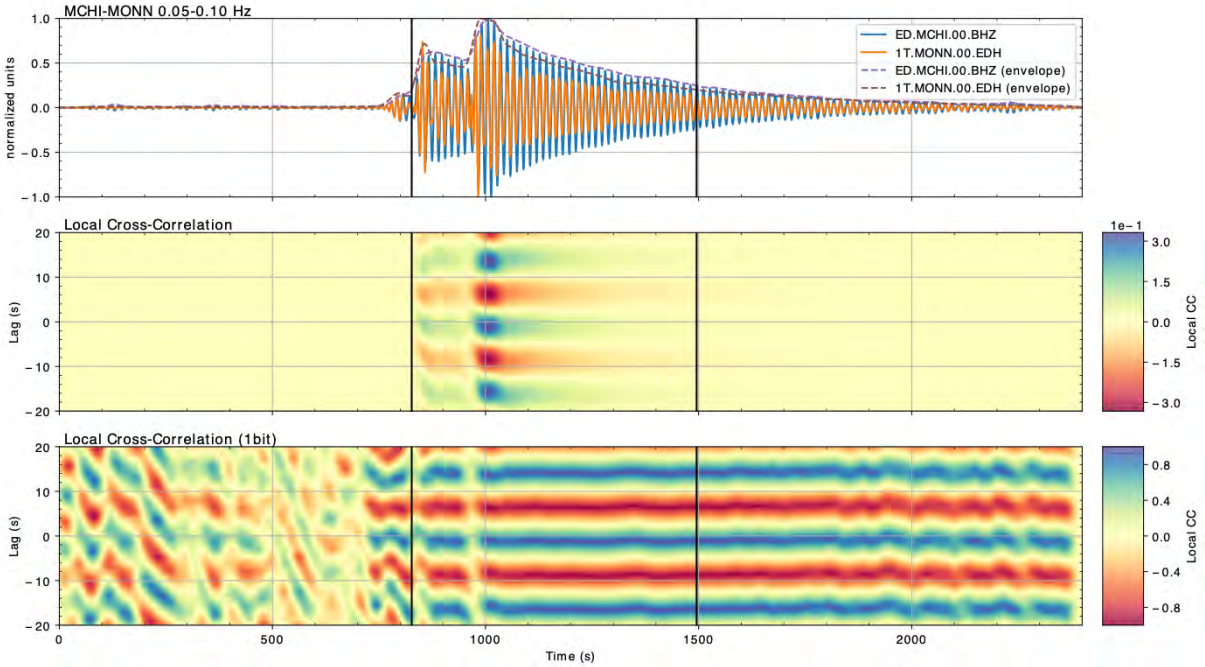

Figure S2.17: Local cross-correlation between ground station MCHI and ocean bottom hydrophone MONN for the February 26, 2019 VLF. (top) Signals filtered between 10 and 20 s (0.05-0.10 Hz) and aligned to the same reference time. The vertical bars indicate the window where the signal envelopes are larger than 20% of their maximum. (middle) Cross-correlation. (bottom) Cross-correlation after 1-bit normalization.

We then back-projected the average 1-bit cross-correlations (CC) over time-delay 3D maps (Poiata, Satriano et al. 2016), assuming a constant wave velocity of 3.5 km/s. Figure S2.18a shows an example of CC maps (2D projection shown) for three station pairs. The final 3D location map was obtained by stacking the 3D maps for all the possible station pairs (Figure S2.18b), and by taking the stack to the power of N (number of stations), while retaining the CC sign (Figure S2.18c), similar to the "equal differential time" location methods (Lomax 2005).

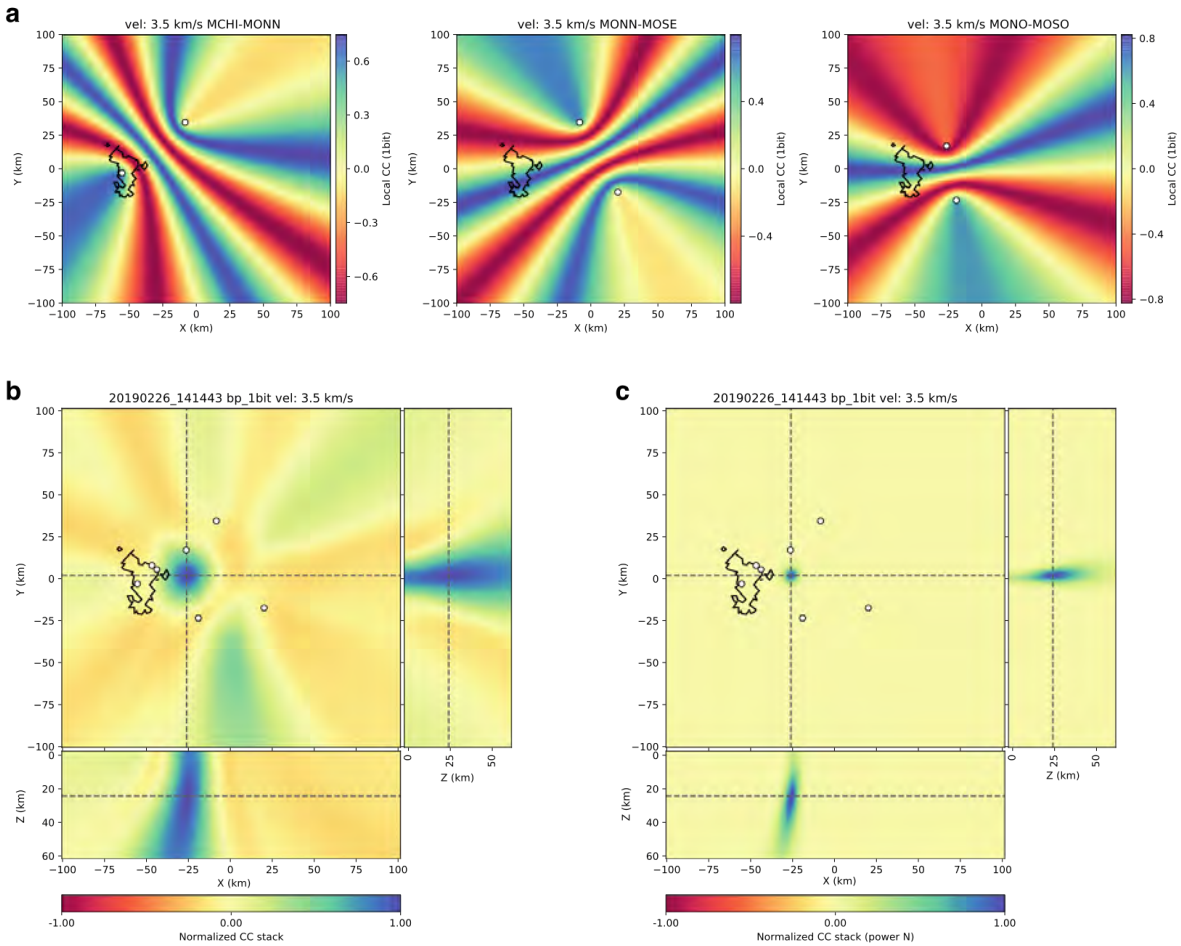

Figure S2.18: Location of the February 26, 2019 VLF. (a) Examples of 2D station delay maps for three station pairs. Station locations are indicated by the white dots. Positive values of cross-correlation (CC) indicate regions for which the signals are in phase; negative values indicate regions for which the signals are in antiphase. (b) and (c) 3D final VLF location maps. For each plot, the horizontal and the two vertical cross sections are taken through the cross-correlation (CC) stack maximum. (b) a stack of all the 3D maps (c) the stack taken to the power of the number of stations.

To the test the effect of different wave speed values on VLF location, we located the VLFs using three different wave velocities in the range of possible S-wave speeds for the region (Dofal, Fontaine et al. 2018): 2.5, 3.5 and 4.5 km/s. The three 3D maps (Figure S2.19) share a well-constrained epicentral location (positive CC stack), with a horizontal 1-sigma error of about 5 km, but the hypocentral depths are significantly different for each velocity. The depth obtained using a velocity of 2.5 km/s is between 29 and 60 km, at which depth S-wave velocity should be faster than 4 km/s (Dofal, Fontaine et al. 2018); The depth obtained using a velocity of 4.5 km/s is between 0 and 23 km, where the S-wave velocity should be slower than 3.5 km/s (Dofal, Fontaine et al. 2018). The most reasonable solution is therefore the one obtained using a wave velocity of 3.5 km/s, which provides a depth between 7 and 40 km.

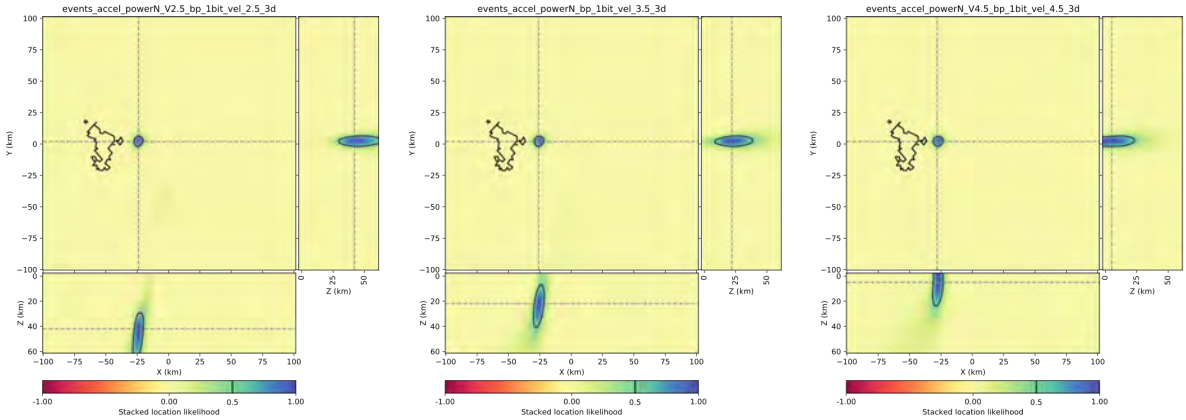

Figure S2.19: Stacked location 3D maps for all the 83 located VLFs, using different wave velocities (2.5, 3.5 and 4.5 km/s). The contour line is at half the maximum stacked CC value, i.e., one sigma. For each plot, the horizontal and the two vertical cross sections are taken through the cross-correlation (CC) stack maximum. Station locations are indicated by the white dots.

S3. Geodesy

See also Extended Data Fig.7.

S3.1 GNSS data and modelling

S3.1.2 Tables

Tables S3.1 presents GNSS displacements and velocities for the study period (January 1, 2018-January 1, 2020) and Tables S3.2 and S3.3 present characteristics of the modelled isotropic and non-isotropic point sources.

Name	Lat N	Lon E	Alt (m)	E (mm)	N (mm)	Up (mm)	dE (mm)	dN (mm)	dU (mm)
BDRL	-12.91	45.193	-4	286.4	103	-202.9	5	5	5
DSUA	-12.30	49.28	22	-8.2	-2.1	29.8	5	5	5
GAMO	-12.76	45.08	-4	265.1	-25.8	-121.7	5	5	5
GLOR	-11.58	47.21	-16	-2.6	0.8	16.6	5	5	7.6
KAWE	-12.76	45.22	12.	299	-36.9	-213.4	5	5	5
KNKL	-12.96	45.10	6	132.4	50.3	-58.9	5.2	5	11.1
MAYG	-12.78	45.25	-16.	265.9	-18.2	-215.4	5	5	5
MTSA	-12.76	45.08	72	269.9	-23.8	-120.9	5	5	5
MTSB	-12.68	45.08	33	152.3	-46.7	-116.3	5	5	10.1
PMZI	-12.80	45.27	-12	146.8	-9.5	-162.9	5	5	8.9
PORO	-12.90	45.14	-6	285.8	71.6	-169.7	5	5	5

Table S3.1: GNSS displacements for the January 1, 2018-January 1, 2020 period

	lon	lat	Z (km)	ΔV_{tot}	Mean error
Source	45.66 E ± 6 km	12.81 S ± 9 km	-39 ± 1 km	-5.5 to 5.2 $(km)^3$	44 mm

Table S3.2: Characteristics of the isotropic point source (location with 1s uncertainties)

	lon	lat	Z (km)	ΔV_{tot}	$\Delta V_Z/\Delta V_{tot}$	$\Delta V_X/\Delta V_{X+Y}$	Ω_X	Ω_Y	Ω_Z	Mean error
Source	45.47 E ± 10 km	-12.79 S ± 1 km	-27 ± 1 km	-5.5 $(km)^3$	0.05	0.48	3	11	-3	37 mm

Table S3.3: Characteristics of the pCDM source (location with 1s uncertainties)

S3.1.2 Modelling

Ground deformation modelling in volcanic areas provides useful quantitative information on the location and shape of magma reservoirs and on the volume of magma circulation at depth (Dvorak and Dzurisin 1997) (Dzurisin 2003) (Segall 2010). Source characteristics driving surface displacements can be retrieved to a first order by modelling a point source in an elastic half-space. This strategy is relevant and robust when the amount of observations is limited. We use two distinct analytical formalisms: 1) an isotropic point source (Anderson 1936) that is often used as an approximation of hydrostatic pressure variation in a deep spherical source (Kiyoo 1958), and 2) a point compound dislocation model (pCDM), a point source approximation of a 3D volumetric source that can model, in the far field, surface displacements due to any triaxial ellipsoidal shapes and degenerate cases like a sill, dyke or sphere (Nikkhoo, Walter et al. 2016). These two types of modelling are operationally used for real-time volcano monitoring in the WebObs system (Beauducel, Lafon et al. 2020), (Beauducel, Peltier et al. 2020), an integrated web-based system for data monitoring and network management implemented in 15 observatories worldwide, including the REVOSIMA (REVOSIMA 2020).

Both models assume a homogeneous elastic half-space, an isotropic material with Poisson's ratio of 0.25, and are only relevant at far-field observation points because of the point source approximation. In our case study, this last assumption is valid because the seismicity, and thus the probable associated source of the surface deformation, is located at depths greater than 20 km. These simple models give a first order estimation of the magnitude and characteristics of the source(s) at the origin of the surface displacements observed on land. The lack of precise surface displacement rates above the source of deformation prevents the use of more elaborate models.

The isotropic point source model provides analytical expressions for surface displacements due to a simple isotropic volume variation and depends on four parameters. The relationship between surface displacements and volume change is given by:

$$U_z = (3\ \Delta V\ d) / (4\ \pi\ (d^2 + r^2))^{1.5} \qquad (1)$$

$$Ur = (3\ \Delta V\ r) / (4\ \pi\ (d^2 + r^2))^{1.5} \qquad (2)$$

Where U_r and U_z are the radial and vertical displacements (in m), respectively, at the surface for an observation point located a radial distance r from the point source (in m), d is the depth of the source centre (in m) and ΔV is the volume change (in m^3).

The pCDM model provides analytical expressions for surface displacements due to a source composed of three mutually orthogonal tensile dislocations, one horizontal and two vertical, freely oriented in space (3 rotational degrees of freedom) in an elastic half-space. The pCDM model depends on 9 parameters: 3 for the hypocentre location (horizontal coordinates and depth), 3 for the volume variations (of the same sign, for each plane) and 3 for the angles of rotation (around each 3-D axis). The ratio between the 3 volume variations on each discontinuity translates the source geometry.

We used data from the stations on Mayotte island, Diego Suarez (DSUA) and Grande Glorieuse (GLOR) (main text Figure 1a and Extended data Fig7, Table S3.1): the KNKL, MTSB, PMZI stations on Mayotte and the distant DSUA, (Madagascar) and GLOR (Grande Glorieuse) stations were installed after the beginning of the crisis (Extended data Figure 7) but give better constraints on the source, notably in far-field for the DSUA and GLOR stations. Surface displacements are estimated using weighted linear trends on the period of observation for each station. This method improves the integration of sparse data from all stations installed in 2019, by extrapolating the velocity trend for 2018 period. In our calculations using surface

displacements (corrected from the pre-eruptive global trend that includes a plate tectonic translation) we invert for the source location, volume variation and, in the case of the pCDM source, the six additional geometry parameters. We perform inversion calculations in a Bayesian framework (Tarantola 1984), exploring all model parameter values and computing a probability function for each possible model based on the misfit. This method describes the "model space" associated with a set of data, an efficient way to properly estimate the confidence in the best-fit model (Beauducel and Carbone 2015). This approach also gives a natural estimation of *a posteriori* uncertainties for each parameter. For the isotropic source, a 4-dimension matrix of parameters is computed with a hundred million forward problems. For the pCDM source, systematic exploration of the model space is not possible. Therefore, we use a Monte Carlo algorithm with ten million forward problems randomly chosen in the 9-parameter model space. *A posteriori* uncertainties of the best model solution are given by the interval of variation over each parameter that keeps 68% (one standard deviation) of the highest model probabilities.

S3.1.3 Inversion results

Test 1, Isotropic point source: We inverted the four parameters of an isotropic point source search for best fit without any *a priori* on the source location or volume variation. We computed trends on time series for all available stations on Mayotte and the two distant stations in Grande Glorieuse and Diego Suarez from January 1, 2018 to January 1, 2020. We found a best-fit source (mean error on displacements of only 44 mm), a deflating point located 40 ± 6 km east of Mayotte, at 39 ± 1 km depth with a volume variation of -5.5 to 5.2 km^3 (see Extended data Figure 7b –GNSS and Supplementary table S3.2).

Test 2, triple volumetric discontinuities -pCDM source: We inverted the nine parameters of a pCDM source to look for the best fit without any *a priori* on the source location or shape. The best-fit solution is a well-constrained sub-vertical pipe 30 ± 3 km east of Mayotte, at 27 ± 1 km

depth and with a volume variation of -5.5 km^3 (see Extended data Figure 7c –GNSS and Supplementary Table S3.3). The particular shape of the source is expressed by a quasi-null volume variation on the horizontal discontinuity, and near equal volume variations on the two vertical discontinuities. This mimics an elongated prolate axisymmetric ellipsoid or a pipe. The vertical orientation is given by the low value of rotation angles around horizontal axis. While the volume variation is similar, the location of this second source differs from the isotropic one. This can be a side effect of the poorly constrained geometry of the GNSS network, or this might evidence the complexity of the real source of deformation, with multiple reservoirs, spatially extended and active simultaneously.

S3.2 Sea floor pressure data:

In addition to on-land GNSS data, sea floor pressure data sensors were deployed on each OBS frame, collecting data from March to May 2019 (see location on Figure S2.1). The pressure records are dominated by a tidal signal with up to 4m amplitude (Extended Data Figure 7d). After removing most of the tides by harmonic analysis using the "UTide" code (Codiga 2011) and low-pass filtering at 36h, the residual signal includes possible seafloor deformation, oceanographic "noise" and instrumental drift. We observed a continuing increase in all the pressure records after the sensors adjusted to the seafloor depth and temperature. We believe that the observed increase corresponds to a seafloor subsidence signal at all the stations. This subsidence is within the expected range of subsidence modelled from on-shore GNSS data. Residual signal after subtracting the model-predicted trend from the seafloor pressure variations probably contains instrumental drift (especially in the first 2 weeks of the deployment) but may also include some mis-modelled seafloor deformation. The residuals at stations MOSE and MONE (see location Figure S2.1) exhibit slight negative and positive trends, respectively which could indicate that the volcanic source is located a bit further south than that modelled using the

GNSS data, assuming that instrumental drift is not the dominant factor. The sea floor pressure data sensors also confirm that there is no significant sudden deformation beneath any of the OBS sites, which is coherent with the lack of shallow earthquakes.

References

An, C., C. Cai, Y. Zheng, L. Meng and P. Liu (2017). "Theoretical solution and applications of ocean bottom pressure induced by seismic seafloor motion." Geophysical Research Letters **44**(20): 10,272-210,281.

Anderson, E. (1936). "Dynamics of formation of cone-sheets, ring-dikes, and cauldron subsidences: Royal Society of Edinburgh Proceedings, v. 56."

Beauducel, F. and D. Carbone (2015). "A strategy to explore the topography-driven distortions in the tilt field induced by a spherical pressure source: the case of Mt Etna." Geophysical Journal International **201**(3): 1471-1481.

Beauducel, F., D. Lafon, X. Béguin, J.-M. Saurel, A. Bosson, D. Mallarino, P. Boissier, C. Brunet, A. Lemarchand and C. Anténor-Habazac (2020). "WebObs: The volcano observatories missing link between research and real-time monitoring." FrEaS **8**: 48.

Beauducel, F., A. Peltier, A. Villié and W. Suryanto (2020). "Mechanical imaging of a volcano plumbing system from GNSS unsupervised modeling." Geophysical Research Letters **47**(17): e2020GL089419.

Chatelain, J. L. (1978). Etude fine de la sismicité en zone de collision continentale au moyen d'un réseau de stations portables: la région Hindu-Kush Pamir, Université scientifique et médicale de Grenoble.

Codiga, D. L. (2011). Unified tidal analysis and prediction using the UTide Matlab functions, Graduate School of Oceanography, University of Rhode Island Narragansett, RI.

Coffin, M. F., P. D. Rabinowitz and R. E. Houtz (1986). "Crustal structure in the western Somali Basin." Geophysical Journal International **86**(2): 331-369.

Dofal, A., F. R. Fontaine, L. Michon, G. Barruol and H. Tkalcic (2018). Crustal structure variation across the southwestern Indian Ocean from receiver functions determined at Ocean-Bottom Seismometers. AGU Fall Meeting 2018, AGU.

Dvorak, J. J. and D. Dzurisin (1997). "Volcano geodesy: The search for magma reservoirs and the formation of eruptive vents." Reviews of Geophysics **35**(3): 343-384.

Dzurisin, D. (2003). "A comprehensive approach to monitoring volcano deformation as a window on the eruption cycle." Reviews of Geophysics **41**(1).

Grevemeyer, I., N. W. Hayman, D. Lange, C. Peirce, C. Papenberg, H. J. Van Avendonk, F. Schmid, L. G. de La Peña and A. Dannowski (2019). "Constraining the maximum depth of brittle deformation at slow-and ultraslow-spreading ridges using microseismicity." Geology **47**(11): 1069-1073.

Gurioli, L., A. Di Muro, I. Vlastélic, S. Moune, S. Thivet, M. Valer, N. Villeneuve, G. Boudoire, A. Peltier and P. Bachèlery (2018). "Integrating field, textural, and geochemical monitoring to track eruption triggers and dynamics: a case study from Piton de la Fournaise." Solid Earth **9**(2): 431.

Hale, D. (2006). "An efficient method for computing local cross-correlations of multi-dimensional signals." CWP Report **656**.

Jochum, K. P., U. Weis, B. Schwager, B. Stoll, S. A. Wilson, G. H. Haug, M. O. Andreae and J. Enzweiler (2016). "Reference values following ISO guidelines for frequently requested rock reference materials." Geostandards and Geoanalytical Research **40**(3): 333-350.

Kennett, B. L., E. Engdahl and R. Buland (1995). "Constraints on seismic velocities in the Earth from traveltimes." Geophysical Journal International **122**(1): 108-124.

Kiyoo, M. (1958). "Relations between the eruptions of various volcanoes and the deformations of the ground surfaces around them." Earthq Res Inst **36**: 99-134.

Lahr, J. C. (1999). HYPOELLIPSE: A computer program for determining local earthquake hypocentral parameters, magnitude, and first motion pattern, US Geological Survey Denver, Colorado.

Larose, E., A. Derode, M. Campillo and M. Fink (2004). "Imaging from one-bit correlations of wideband diffuse wave fields." Journal of Applied Physics **95**(12): 8393-8399.

Lee, W. H. K. and J. C. Lahr (1972). HYPO71: A computer program for determining hypocenter, magnitude, and first motion pattern of local earthquakes, US Department of the Interior, Geological Survey, National Center for ….

Lomax, A. (2005). "A reanalysis of the hypocentral location and related observations for the great 1906 California earthquake." Bulletin of the Seismological Society of America **95**(3): 861-877.

Lomax, A., A. Michelini and A. Curtis (2009). "Earthquake location, direct, global-search methods." Encyclopedia of complexity and system science **5**: 1-33.

Nikkhoo, M., T. R. Walter, P. R. Lundgren and P. Prats-Iraola (2016). "Compound dislocation models (CDMs) for volcano deformation analyses." Geophysical Journal International: ggw427.

Poiata, N., C. Satriano, J.-P. Vilotte, P. Bernard and K. Obara (2016). "Multiband array detection and location of seismic sources recorded by dense seismic networks." Geophysical Journal International **205**(3): 1548-1573.

REVOSIMA, R. d. s. V. e. S. d. M. (2020). "Bulletin n°16 de l'activité sismo-volcanique à Mayotte, du 1 au 31 mars 2020."

Segall, P. (2010). Earthquake and volcano deformation, Princeton University Press.

Tarantola, A. (1984). "Linearized inversion of seismic reflection data." Geophysical prospecting **32**(6): 998-1015.

Weber, B., J. Becker, W. Hanka, A. Heinloo, M. Hoffmann, T. Kraft, D. Pahlke, J. Reinhardt, J. Saul and H. Thoms (2007). SeisComP3—Automatic and interactive real time data processing. Geophysical Research Abstracts.

Withers, M., R. Aster, C. Young, J. Beiriger, M. Harris, S. Moore and J. Trujillo (1998). "A comparison of select trigger algorithms for automated global seismic phase and event detection." Bulletin of the Seismological Society of America **88**(1): 95-106.